Cell Reports

Article

The synaptic basis of activity-dependent eye-specific competition

Graphical abstract

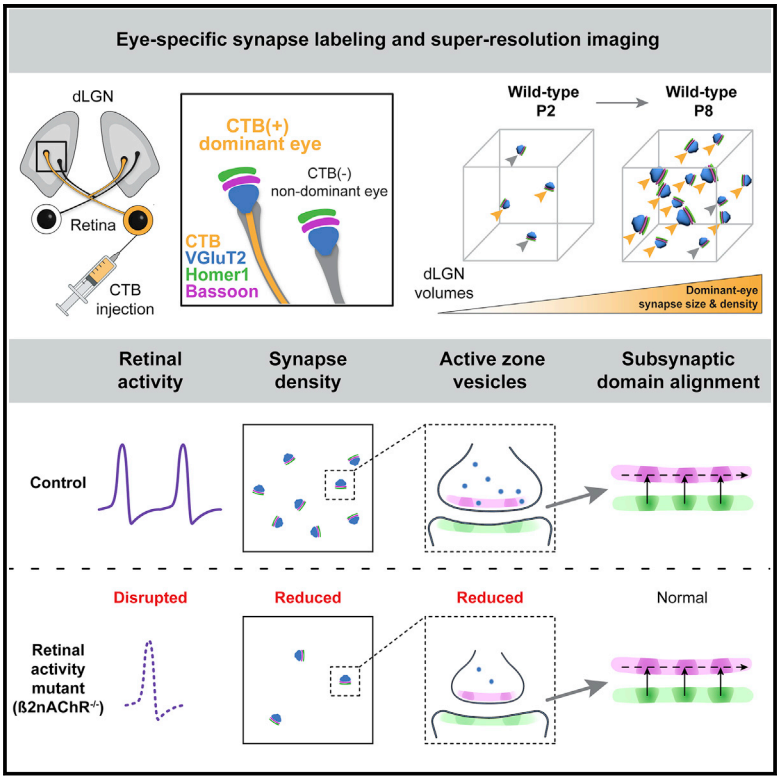

Highlights

- Four-color volumetric super-resolution imaging of eye-specific synapse development
- Eye-specific synapses show activity-dependent differences in presynaptic maturation
- Abnormal retinal wave activity disrupts vesicle organization at the active zone
- Subsynaptic domain alignment is independent of eye of origin and retinal activity

Authors

Chenghang Zhang, Swapnil Yadav, Colenso M. Speer

Correspondence

cspeer@umd.edu

In brief

Zhang et al. use volumetric single-molecule localization super-resolution microscopy to investigate eye-specific synaptic competition in the developing mammalian visual system. Retinogeniculate segregation involves eye-specific changes in synapse density, synapse size, and vesicle organization at the active zone that are disrupted in a genetic mutant with abnormal spontaneous retinal activity.

Zhang et al., 2023, Cell Reports *42*, 112085
February 28, 2023
https://doi.org/10.1016/j.celrep.2023.112085

Cell Reports

CellPress
OPEN ACCESS

Article

The synaptic basis of activity-dependent eye-specific competition

Chenghang Zhang,[1] Swapnil Yadav,[1] and Colenso M. Speer[1,2,*]
[1]Department of Biology, University of Maryland, College Park, MD 20742, USA
[2]Lead contact
*Correspondence: cspeer@umd.edu
https://doi.org/10.1016/j.celrep.2023.112085

SUMMARY

Binocular vision requires proper developmental wiring of eye-specific inputs to the brain. In the thalamus, axons from the two eyes initially overlap in the dorsal lateral geniculate nucleus and undergo activity-dependent competition to segregate into target domains. Here, we combine eye-specific tract tracing with volumetric super-resolution imaging to measure the nanoscale molecular reorganization of developing retinogeniculate eye-specific synapses in the mouse brain. We show there are eye-specific differences in presynaptic vesicle pool size and vesicle association with the active zone at the earliest stages of retinogeniculate refinement but find no evidence of eye-specific differences in subsynaptic domain number, size, or transsynaptic alignment across development. Genetic disruption of spontaneous retinal activity decreases retinogeniculate synapse density, delays the emergence eye-specific differences in vesicle organization, and disrupts subsynaptic domain maturation. These results suggest that activity-dependent eye-specific presynaptic maturation underlies synaptic competition in the mammalian visual system.

INTRODUCTION

The refinement of eye-specific projections to the dorsal lateral geniculate nucleus (dLGN) of the thalamus is a classic model system for investigating the role of spontaneous neural activity in synaptic competition during mammalian brain development.[1–4] In the mouse, retinal ganglion cell (RGC) axons from the left and right eyes innervate the dLGN and then segregate into eye-specific domains prior to eye opening.[5] Eye-specific segregation is regulated by cholinergic spontaneous activity in the eyes ("retinal waves") during the first postnatal week[6,7] and pharmacological disruptions of retinal waves cause defects in eye-specific axon segregation.[8–20] Similar activity-dependent defects have been shown following genetic deletion of the β2 subunit of the nicotinic acetylcholine receptor (β2NAChR$^{-/-}$) which disrupts cholinergic retinal waves and arrests eye-specific segregation.[17,21–28]

Activity-dependent anatomical defects in eye-specific refinement are routinely studied by imaging bulk-labeled RGC axons using anterograde tracers or fluorescent protein expression.[2] Additionally, single axon labeling experiments demonstrate that axonal refinement proceeds by the addition of branches in the correct target termination zone together with the elimination of small side branches.[21,29–33] The results of these experiments have established our current understanding of activity-dependent binocular competition with little information regarding synaptic molecular development and remodeling. A direct analysis of eye-specific synaptic competition has been hindered by difficulties in identifying immature retinogeniculate synapses based on ultrastructural features in electron microscopy (EM) images.[34] At the same time, the diffraction limit of conventional light microscopy precludes fluorescence imaging analysis of synaptic organization at the nanoscale.[35] Thus, although eye-specific segregation is a long-standing model system for exploring activity-dependent circuit refinement, the synaptic basis of eye-specific retinogeniculate competition is unknown.

To address this gap, we combined eye-specific anterograde tracing with volumetric super-resolution microscopy and pre-/postsynaptic immunolabeling *in situ* to measure nanoscale structural properties of 82,892 retinogeniculate synapses during eye-specific competition in the first postnatal week in the mouse (P2–P8). To determine the impact of disrupted spontaneous retinal activity on eye-specific refinement, we compared normal development in wild-type (WT) mice with disrupted refinement in β2NAChR$^{-/-}$ transgenic mice (hereafter referred to as β2$^{-/-}$). During retinogeniculate development in WT animals, we measured early (P2–P4) eye-specific differences in the maturation of presynaptic vesicle pool size and association with the active zone (AZ) that were correlated with the future outcome of eye-specific competition. Compared with WT, β2$^{-/-}$ mice showed no developmental changes in retinogeniculate synapse density and lacked early eye-specific differences in vesicle association with the AZ. In contrast to activity-dependent and eye-specific vesicle pool development, we found no evidence for eye-specific differences in the number of Bassoon or Homer1 subsynaptic domains (SSDs), SSD properties, or transsynaptic SSD alignment across all developmental ages (P2–P8) in either WT or β2$^{-/-}$ mice.

RESULTS

Spontaneous retinal activity regulates eye-specific synapse density

To identify eye-specific synapses, we injected fluorescent anterograde tracer (cholera toxin subunit beta conjugated with Alexa Fluor 488 [CTB]) into the right eye and imaged both the contralateral and ipsilateral regions within the left dLGN before (P2), during (P4), and toward the close (P8) of eye-specific segregation (Figure 1A; see STAR Methods and Figure S1A for contra- and ipsilateral region-of-interest [ROI] selection). We used a serial-section single-molecule localization imaging approach based on stochastic optical reconstruction microscopy (STORM) to collect three-dimensional (3D) super-resolution fluorescence imaging volumes (~45,000 μm^3 each) from each dLGN sample (Figures 1B and S1A).[36] To label retinogeniculate synapses, we immunostained tissue with antibodies against the presynaptic proteins vesicular glutamate transporter 2 (VGluT2, expressed in RGC terminals)[37–40] and Bassoon together with the postsynaptic protein Homer1 (Figure 1B).

The 4-color (Bassoon, Homer1, VGluT2, and CTB) volumetrically aligned image stacks were thresholded and fluorescent signals in STORM images were identified as protein clusters on the basis of size and signal density criteria (see STAR Methods). Retinogeniculate synapses were then identified by the ordered relationship of VGluT2-Bassoon-Homer1 signals in 3D images (Figures 1B and 1C). In this experimental design, CTB colocalization with presynaptic vesicle pools marked right-eye CTB(+) synapses, while left-eye synapses were CTB(−) (Figure 1C). To confirm that anterograde tracing with CTB labels the majority of synapses from the injected eye, we performed control experiments using binocular CTB injections to label all retinogeniculate synapses and then quantified their association with CTB signals. At P2 the majority (~85%) of VGluT2(+) presynaptic clusters were CTB(+) following binocular injections and this further increased from P4 (~94%) to P8 (~98%) demonstrating high-efficiency CTB labeling of retinogeniculate synapses by anterograde tract tracing (Figure S1B).

Using monocular CTB injections to differentiate left- versus right-eye retinogeniculate synapses, we first quantified developmental changes in eye-specific synapse density within eye-specific territories (Figure S1A; STAR Methods). We defined dominant- versus non-dominant-eye inputs on the basis of eye of origin according to the pattern of adult wild-type contra-/ipsilateral eye-specific projections. In the contralateral region of WT mice, the density of CTB(+) dominant-eye (contralateral) synapses increased progressively from P2 to P8 (Figure 1D, left panel; Figure S1B). The density of CTB(−) non-dominant-eye (ipsilateral) synapses initially increased from P2 to P4 (Figure 1D, left panel; Figure S1B), consistent with delayed ipsilateral axon ingrowth.[5] This was followed by significant synapse elimination that resulted in a ~31% reduction in CTB(−) synapse density from P4 to P8 (Figure 1D, left panel; Figure S1B).

Within the ipsilateral region, the density of dominant CTB(−) ipsilateral-eye synapses also increased from P2 to P4 and was stable from P4 to P8 (Figure 1E, left panel; Figure S1B). In contrast, CTB(+) non-dominant contralateral-eye synapse density was stable from P2 to P4 and decreased by ~72% at P8 (Figure 1E, left panel; Figure S1B). Compared with WT mice, synapse density from both eyes did not change across development in $\beta2^{-/-}$ mice (Figures 1D and 1E, right panels). To rule out the impact of developmental expansion of the dLGN on synapse density measurements,[37,41] we quantified cell body density and neuropil fraction within each imaged region across ages/genotypes. We found no significant differences between WT and $\beta2^{-/-}$ animals at any ages (Figure S1C), indicating that the measured differences in synaptic densities reflect a failure of retinogeniculate synapse development in $\beta2^{-/-}$ mice.

Spontaneous retinal activity regulates eye-specific presynaptic vesicle organization

A previous EM study of retinogeniculate refinement in the cat found that nascent synapses formed by individual axons in the non-dominant eye-specific layer contained fewer vesicles compared with synapses formed in the future dominant-eye layer.[29] To further investigate eye-specific and activity-dependent developmental differences in vesicle pool maturation, we quantified the size (volume) and protein enrichment (total signal intensity) of eye-specific VGluT2 clusters in both WT and $\beta2^{-/-}$ mice from P2 to P8 (Figures 2A and S2A). We focused our analysis on synaptic development within the contralateral ROI, which is reliably identified across all ages and genotypes (see STAR Methods). In WT mice, presynaptic VGluT2 clusters from both eyes grew larger (Figure 2B) and contained more VGluT2 proteins (Figure S2A) over development. Across all ages, CTB(+) dominant-eye VGluT2 clusters were larger and contained more proteins than CTB(−) non-dominant-eye clusters (Figures 2B and S2A). In $\beta2^{-/-}$ mice, dominant-eye VGluT2 cluster size also increased over development (Figures 2B and S2A). However, the magnitudes of eye-specific differences at P2 and P4 were reduced at each age compared with WT (Figures 2B and S2A). In WT mice, the median dominant-eye VGluT2 cluster volumes were 140% (P2) and 170% (P4) larger than non-dominant-eye VGluT2 clusters. In $\beta2^{-/-}$ mice, the magnitudes of eye-specific differences in volumes were reduced to 97% (P2) and 73% (P4) (Figure 2B).

Because synaptic strength depends in part on the number of presynaptic release sites as well as docked vesicles,[42] we reasoned that eye-specific synapses may show differences in vesicle pool organization near the AZ. To test this, we measured VGluT2 signal volume and protein enrichment within a 48 nm shell surrounding each AZ Bassoon cluster to quantify vesicles associated with the AZ (Figure 2C; see STAR Methods). Here again we confined our analysis to the contralateral ROI and found that in WT mice, the volume and protein enrichment of AZ-associated VGluT2 signal increased over development for both CTB(+) and CTB(−) synapses (Figures 2D and S2B). In WT mice from P2 to P4, VGluT2 association with the AZ was significantly greater for dominant-eye inputs compared with non-dominant-eye synapses (Figures 2D and S2B). In contrast, $\beta2^{-/-}$ mutants showed no early eye-specific differences in VGluT2 signal near the AZ (Figures 2D and S2B). To rule out the possibility that the measured increase in AZ vesicle signal in WT animals was caused by differences in Bassoon cluster area and corresponding shell volume, we normalized VGluT2

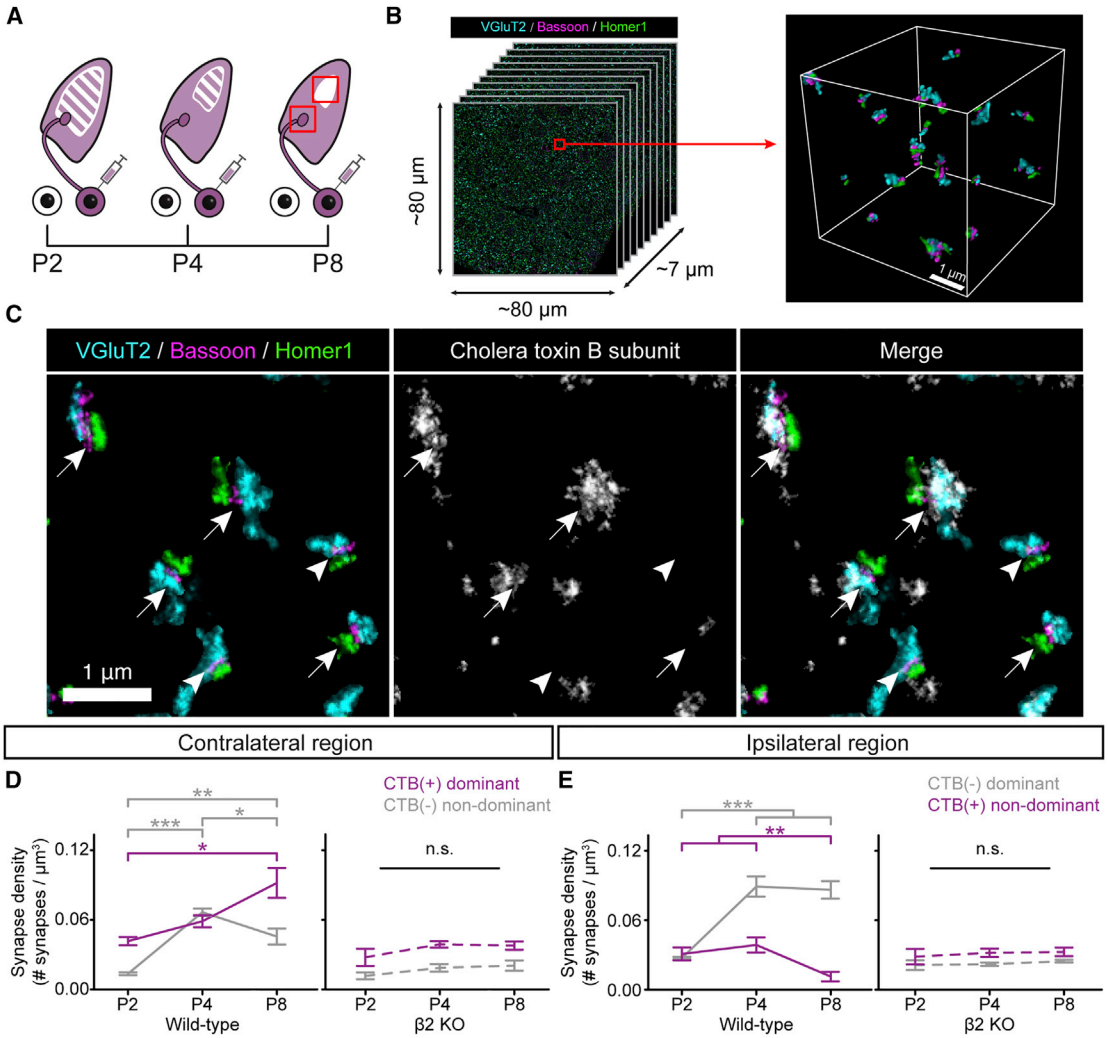

Figure 1. Spontaneous retinal activity regulates eye-specific synapse density

(A) Overview of the experimental design. CTB was injected to the right eye to label contralateral projections and eye-specific synapse development was imaged in two regions of interest (red boxes) at three postnatal time points (P2, P4, and P8) in the left dLGN.

(B) Volumetric super-resolution imaging approach. Individual STORM image stacks (left panel, cartoon not to scale) were ~45,000 μm^3 for each region of interest (contralateral and ipsilateral ROIs), genotype (WT versus $\beta2^{-/-}$ mice), and biological replicate (n = 3 animals). Retinogeniculate synapses were identified in 3D volumetrically aligned image stacks (right panel shows a representative volume of ~104 μm^3 within a P8 contralateral ROI).

(C) Four color super-resolution images of eye-specific retinogeniculate synapses. Representative maximum-intensity Z projection (700 nm) STORM images of synaptic proteins (left panel), CTB signals (middle panel), and merged (right panel) images from P8 WT dLGN in the contralateral ROI. CTB signals colocalized with VGluT2 immunostaining in retinogeniculate synapses. Each imaging volume contained CTB(+) synapses from contralateral axons (arrows) and CTB(−) synapses from ipsilateral axons (arrowheads).

(D) Quantification of activity-dependent eye-specific synapse development in the contralateral ROI. Synapse development trajectories differ between CTB(+) dominant-eye (purple line, left panel) and CTB(−) non-dominant-eye projections (gray line, left panel). Overall synapse density is reduced in $\beta2^{-/-}$ mice and there were no differences in eye-specific densities (dashed lines, right panel). Error bars reflect mean ± SEM from n = 3 biological replicates at each age. Statistical analysis was performed using a one-way ANOVA with a post hoc Tukey test: *$p < 0.05$, **$p < 0.01$, and ***$p < 0.001$. Statistical comparisons over development for each eye of origin are shown in their corresponding colors (purple or gray). n.s., no significant differences were detected across developmental ages.

(E) Quantification of activity-dependent eye-specific synapse development in the ipsilateral ROI. Results are presented as in (D).

signals within the shell to the total shell volume. After normalization we again found early eye-specific differences in AZ-associated VGluT2 in WT, but not $\beta2^{-/-}$ mice (Figures S2C and S2D).

Interestingly, not all AZ Bassoon clusters contained VGluT2 signal within the shell region (Figure 2E). Such "null" synapses with no AZ-associated vesicles may have reduced release probability or be functionally silent.[43] In WT mice at early stages of eye-specific synaptic refinement (P2–P4), projections from the CTB(−) non-dominant-eye showed a higher fraction of "null" synapses compared with the CTB(+) dominant-eye projections (Figure 2F). This early bias in eye-specific competition was resolved by P8 when the fraction of "null" synapses decreased

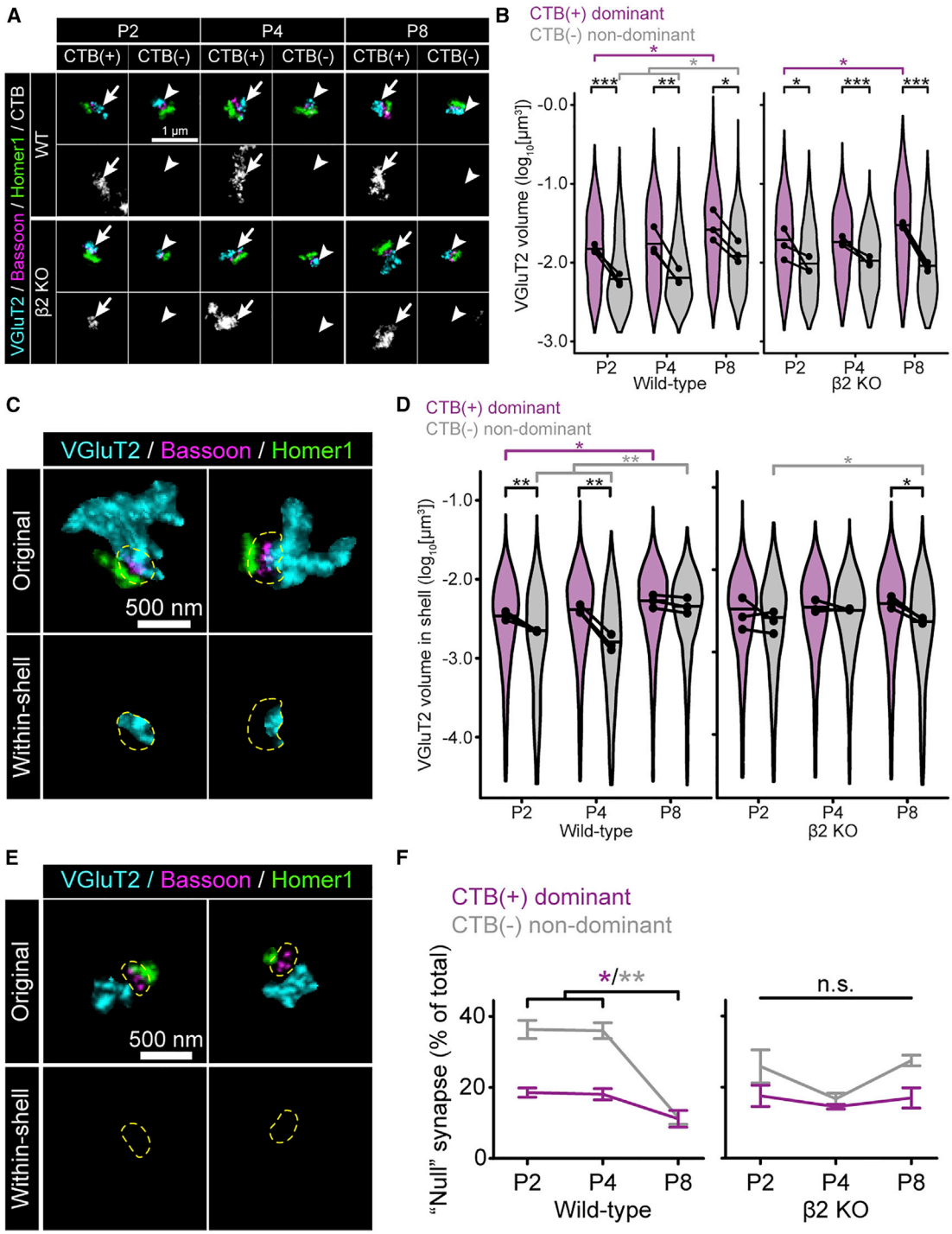

Figure 2. Spontaneous retinal activity regulates eye-specific presynaptic vesicle organization

(A) Representative CTB(+) (arrows) and CTB(−) (arrowheads) retinogeniculate synapses for each age and genotype. Each image is a maximum-intensity Z projection of 210–490 nm. Synaptic proteins are shown in colors and CTB is shown in white. For each age, synapses were selected on the basis of the median value of the VGluT2 volume.

(B) Eye-specific developmental changes in VGluT2 cluster volume in WT (left panel) and $\beta2^{-/-}$ mice (right panel). Violin plots show the full distribution of cluster volume from 3 biological replicates imaged in the contralateral ROI. Horizontal lines show the median values of the grouped data. Black dots reflect the individual median values for each biological replicate. Black lines between CTB(+) and CTB(−) populations represent data collected from the same biological replicate. Statistical analysis was performed using a mixed-model ANOVA where age or eye of origin was the fixed main factor, and the biological replicate ID was a random nested factor. Pairwise comparisons between ages were performed using a post hoc Bonferroni test. Black asterisks indicate statistical comparison between

(legend continued on next page)

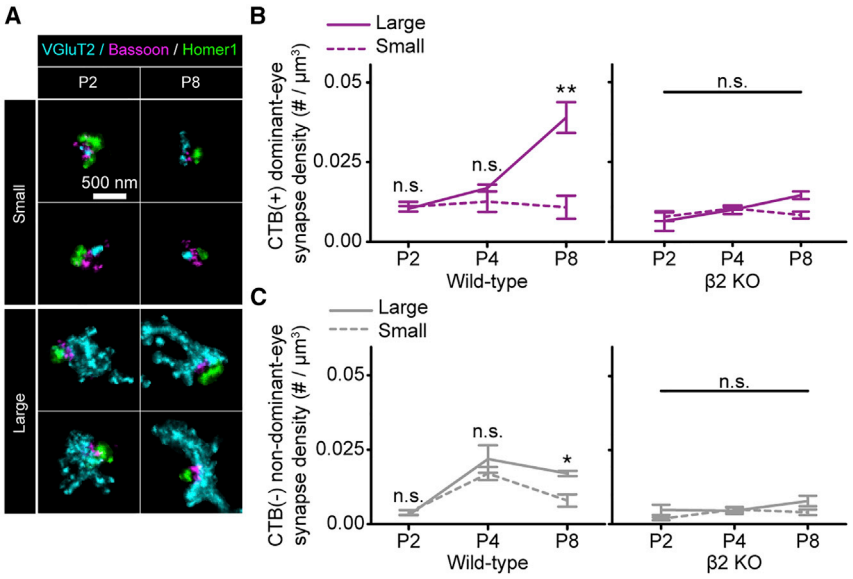

Figure 3. Synapses with larger presynaptic vesicle pools are more abundant after eye-specific competition

(A) Representative small (top panels) and large (bottom panels) retinogeniculate synapses from WT mice at P2 (left panels) and P8 (right panels). Maximum-intensity Z projection images (210–490 nm) show synapses from the contralateral ROI.

(B) Changes in large versus small synapse density from the CTB(+) dominant-eye during development. The line graphs show the density of large (solid purple lines) and small (dashed purple lines) synapses in WT (left panel) and $\beta2^{-/-}$ mice (right panel) measured within the contralateral ROI. Error bars reflect mean ± SEM from n = 3 biological replicates. Statistical analysis was performed using a one-way ANOVA. *p < 0.05 and **p < 0.01., n.s., no significant differences were found between large and small synapses.

(C) Changes in large versus small synapse density from the CTB(−) non-dominant-eye during development. The line graphs show the density of large (solid gray lines) and small (dashed gray lines) synapses in WT (left panel) and $\beta2^{-/-}$ mice (right panel) measured within the contralateral ROI. Error bars reflect mean ± SEM from n = 3 biological replicates. Statistical analysis was performed using a one-way ANOVA. *p < 0.05 and **p < 0.01. n.s., no significant differences were found between large and small synapses.

and reached the same level for both CTB(+) and CTB(−) synaptic populations (Figure 2F). In contrast, $\beta2^{-/-}$ mutants showed no differences in "null" synapse ratios across ages for either eye of origin (Figure 2F). Together, these results show that vesicle association with the presynaptic AZ is developmentally regulated, activity dependent, and eye specific.

Synapses with larger presynaptic vesicle pools are more abundant after eye-specific competition

The difference in presynaptic vesicle content between dominant-eye versus non-dominant-eye synapses (Figures 2A and 2B) suggests that vesicle pool size could be essential for synaptic refinement. To test this idea, we measured the presynaptic VGluT2 volume distribution across each age/genotype and found these were well represented by a two-peak Gaussian function reflecting the presence of two distinct synaptic populations (small versus large) (Figures S3A and S3B; $R^2 > 0.96$ for all fits). We conservatively defined VGluT2 clusters with volumes smaller than the lower peak as a "small" synapse population and those larger than the upper peak as a "large" synapse population (Figure S3B). The synapse classification was consistent across ages/genotypes (Figure S3C) and large/small eye-specific VGluT2 clusters were morphologically similar across all conditions (Figure 3A).

Comparing the synapse density of the two populations in WT mice (Figures 3B and 3C, left panels), we found that the overall increase in VGluT2 cluster volume in CTB(+) dominant-eye synapses (Figure 2B) reflected an increase in the density of large synapses while the density of small synapses did not change from P2 to P8 (Figure 3B, left panel). Consistent with the increase in ipsilateral-eye synapse density at P4 (Figures 1D and S1B), the density of both large and small CTB(−) non-dominant-eye synapses increased from P2 to P4 (Figure 3C, left panel). Subsequently from P4 to P8, the density of both large and small CTB(−) non-dominant-eye synapses decreased, but the loss of small synapses was more significant (~50% decrease)

eye-specific CTB(+) and CTB(−) clusters. Purple asterisks indicate statistical comparisons between CTB(+) clusters across ages. Gray asterisks indicate statistical comparisons of CTB(−) clusters across ages. *p < 0.05, **p < 0.01, and ***p < 0.001.

(C) Analysis of active zone-associated VGluT2 volume. VGluT2 signal was measured within a 48 nm shell (dashed yellow line) surrounding presynaptic Bassoon clusters. Maximum-intensity Z projection images (210–490 nm) show representative P8 WT synapses from the contralateral ROI.

(D) Eye-specific VGluT2 volume at the AZ in WT (left panel) and $\beta2^{-/-}$ mice (right panel) across development. Violin plots show the grouped distribution of cluster volumes from 3 biological replicates imaged in the contralateral ROI. Horizontal lines show the median values of the grouped data. Black dots reflect the individual median values for each biological replicate. Black lines between CTB(+) and CTB(−) populations represent data collected from the same biological replicate sample. Statistical analysis was performed using a mixed-model ANOVA where age or eye of origin was the fixed main factor, and the biological replicate ID was a random nested factor. Pairwise comparisons between ages were performed using a post hoc Bonferroni test. Black asterisks indicate statistical comparison between eye-specific CTB(+) and CTB(−) clusters. Purple asterisks indicate statistical comparisons between CTB(+) clusters across ages. Gray asterisks indicate statistical comparisons between CTB(−) clusters across ages. *p < 0.05, **p < 0.01, and ***p < 0.001.

(E) STORM images of "null" synapses with no AZ-associated vesicles. VGluT2 signal was measured within a 48 nm shell (dashed yellow line) surrounding presynaptic Bassoon clusters. Maximum-intensity Z projection images (210–490 nm) show representative P8 WT synapses from the contralateral ROI.

(F) The fraction of "null" synapses in WT (left panel) and $\beta2^{-/-}$ mice (right panel) across development. The line graphs show grouped distribution of "null" synapse fraction from 3 biological replicates imaged in the contralateral ROI. Error bars reflect mean ± SEM. Statistical analysis was performed using a one-way ANOVA with a post hoc Tukey test. *p < 0.05 and **p < 0.01. n.s., no significant differences were detected across developmental ages.

compared with larger synapses (~17% decrease) (Figure 3C, left panel). We found no developmental changes in the density of large versus small synapses of either eye of origin in $\beta2^{-/-}$ mutants (Figures 3B and 3C), demonstrating an activity-dependent failure of presynaptic vesicle pool maturation underlying eye-specific competition.

Subsynaptic domain development is independent of eye of origin

Super-resolution imaging enables the detection of SSDs that coordinate presynaptic release with postsynaptic receptors during neurotransmission.[44,45] To investigate whether SSDs in retinogeniculate synapses show developmental or eye-specific differences, we identified pre-/postsynaptic SSDs on the basis of voxel intensity distributions in 3D-aligned STORM images (Figure 4A, "image-based analysis"). After separating SSDs by watershedding, we measured SSD properties within retinogeniculate Bassoon and Homer1 clusters in the contralateral ROI (see STAR Methods).

The average number of Bassoon or Homer1 SSDs per synapse was between 2 and 3 across our retinogeniculate synapse dataset (Figure 4B). The number of Bassoon SSDs in each synapse (Figure 4B, top panels) was largely consistent across development and showed no eye-specific differences in either WT or $\beta2^{-/-}$ mice. Postsynaptically, the number of Homer1 SSDs per synapse decreased from P4 to P8 in WT mice (Figure 4B, bottom left panel), while $\beta2^{-/-}$ mice showed an opposite developmental pattern (Figure 4B, bottom right panel) indicating activity-dependent developmental changes in postsynaptic Homer1 distribution. However, similar to Bassoon SSDs, we found no eye-specific differences in the number of Homer1 SSDs per synapse across ages and genotypes (Figure 4B, bottom panels). We next quantified the volume and signal intensity of Bassoon and Homer1 SSDs for all synapses in our dataset and found no developmental (data not shown) or eye-specific changes for either genotype (Figure 4C).

To further investigate SSD properties on the basis of single-molecule localization density information, we developed a machine learning approach to reconstruct single-molecule localization distributions from volumetrically aligned STORM images. We trained a convolutional neural network (CNN) model using unaligned two-dimensional (2D) STORM images and the corresponding ground truth single-molecule distributions (see STAR Methods). The model was then applied to predict localization distributions from 3D-aligned STORM images and SSDs were identified by density-based spatial clustering of applications with noise (DBSCAN) analysis (Figure S4A). To evaluate the SSD detection accuracy within the CNN-predicted output, we compared the centroid positions of SSDs identified within ground truth 2D STORM localization distributions versus their corresponding CNN predictions (see STAR Methods). We found short offsets between SSD centroid positions across the comparison (~21–29 nm) indicating that SSDs identified by the model were in good agreement with ground truth data (Figure S4B). Consistent with the image-based analysis, we found no eye-specific differences in SSD number (Figure S4C) or volume (Figure S4D) across ages or genotypes.

Pre-/postsynaptic SSDs are aligned in "nanocolumns" that position presynaptic release sites close to postsynaptic receptors for efficient neurotransmission.[45] Based on this arrangement, we reasoned that transsynaptic SSD alignment could be regulated as a mechanism for eye-specific refinement. To test this, we performed an alignment analysis to measure Bassoon and Homer1 SSD spatial relationships across our entire synaptic dataset for all ages and genotypes. After determining the optimal parallel plane of pre-/postsynaptic alignment, we measured the displacement between SSD weighted centroid positions relative to a perpendicular vector across each synapse (Figure 4D; see STAR Methods). The average SSD displacement (~100 nm) was significantly smaller than control measurements in which we randomized postsynaptic SSD positions within each individual synapse (Figure 4E). We found no significant differences in transsynaptic SSD alignment between age groups, genotype (Figure 4E), or eye of origin (data not shown), suggesting that transsynaptic SSD alignment is robust during activity-dependent synaptic refinement.

DISCUSSION

Previous work has shown significant defects in eye-specific axon refinement resulting from manipulations of spontaneous retinal activity. Such changes are expected to affect retinogeniculate microcircuit development, yet little is known about the synaptic basis of activity-dependent competition during eye-specific segregation. Here we used volumetric super-resolution imaging to measure the activity-dependent development of eye-specific synapses with molecular labeling information and subsynaptic image resolution. By analyzing tens of thousands of developing eye-specific synapses we found that (1) genetically disrupting spontaneous retinal activity causes a significant decrease in retinogeniculate synapse density underlying failed eye-specific refinement; (2) presynaptic vesicle pool maturation and subsynaptic association with the AZ are activity dependent and show eye-specific differences correlated with synaptic competition outcomes; (3) there are no eye-specific differences in the SSD organization of AZ (Bassoon) and postsynaptic density (Homer1) proteins during development; and (4) there are no developmental, eye-specific, or activity-dependent differences in transsynaptic SSD alignment in retinogeniculate synapses during eye-specific refinement. Together, these results show that eye-specific presynaptic vesicle pool maturation underlies activity-dependent synaptic competition mechanisms *in vivo*.

Molecular mechanisms underlying eye-specific presynaptic vesicle pool maturation

Our four-channel super-resolution images revealed significant developmental and activity-dependent differences in vesicle pool maturation and enrichment at the AZ that differentiated eye of origin in the developing dLGN (Figure 2). These findings are consistent with a previous ultrastructural study of prenatal retinogeniculate development in the cat in which more synaptic vesicles were found in dominant versus non-dominant eye-specific presynaptic terminals.[29] A possible mechanism for eye-specific vesicle pool maturation is the induction of cyclic

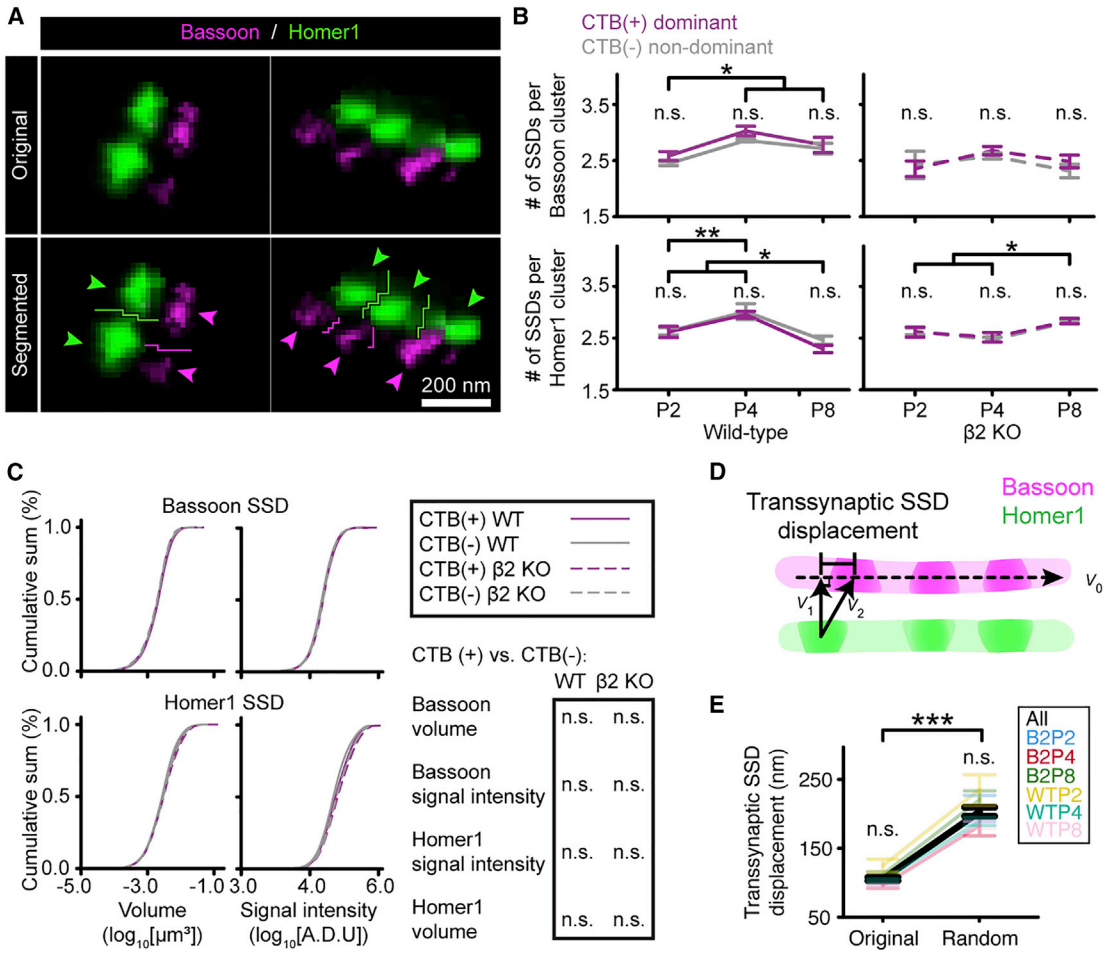

Figure 4. Subsynaptic domain maturation is independent of eye of origin

(A) Subsynaptic domain (SSD) identification in STORM images. From STORM images (top panels), Bassoon (purple arrowheads) and Homer1 (green arrowheads) SSDs were separated by watershedding at local image intensity minima (colored lines). Representative images show the middle section of each 3D cluster from a P8 WT sample in the contralateral ROI.

(B) Changes in synaptic SSD number during development. Line graphs show the change in SSD number in Bassoon (top panels) and Homer1 (bottom panels) in WT (left panels) and $\beta2^{-/-}$ mice (right panels) over development. Purple lines reflect CTB(+) dominant-eye synapses while gray lines reflect CTB(−) non-dominant-eye synapses. Error bars show mean ± SEM from n = 3 biological replicates. Statistical analysis was performed using a one-way ANOVA with a post hoc Tukey test. *$p < 0.05$ and **$p < 0.01$. n.s., not significant.

(C) No eye-specific differences in SSD properties during retinogeniculate segregation. Cumulative histograms show SSD volume (left panels) and signal intensity (right panels) for all Bassoon (top panels) and Homer1 (bottom panels) clusters. Each histogram shows grouped data for all synapses across development (P2/P4/P8; n = 3 biological replicates for each age). Statistical analysis was performed using a mixed-model ANOVA where the eye of origin was the fixed main factor, and the biological replicate ID was a random nested factor. A summary of statistical comparisons between CTB(+) and CTB(−) clusters for both WT and $\beta2^{-/-}$ mice (bottom right) shows no significant differences. n.s., not significant.

(D) Illustration of transsynaptic SSD displacement measurement. The cartoon shows paired Bassoon (magenta) and Homer1 (green) SSDs (darker colored regions) within a synapse (lighter colored background). For the analysis of each individual SSD pair, v_0 is a vector through the principal plane of the Bassoon cluster. v_1 is a vector perpendicular to v_0. v_2 is a vector that runs from the centroid of the Homer1 SSD to the centroid of the nearest Bassoon SSD within the synapse. After aligning the tails of v_1 and v_2 to the same origin, the transsynaptic SSD displacement was calculated by measuring the distance between the intersections of v_1 and v_2 with v_0.

(E) No changes in transsynaptic SSD displacement across ages and genotypes. Colored lines show mean transsynaptic SSD displacement from 3 biological replicates for each age and genotype (data are grouped from both eyes, which showed no eye-specific differences). The black line shows grouped data of all ages and genotypes for both eyes. Error bars reflect mean ± SEM. Statistical analysis was performed using a one-way ANOVA. n.s., no significant differences between genotypes, ages, or eye of origin within original and randomized measurements. ***Significant difference in displacement comparing original SSDs versus randomized data ($p < 0.001$). n.s., no significant differences were detected across developmental ages and genotypes.

AMP/protein kinase A (cAMP-PKA) signaling by Ca^{2+}-dependent adenylyl cyclase (AC) activity.[46] AC1 mutant mice ($AC1^{-/-}$) show disrupted eye-specific retinogeniculate segregation[47,48] resulting from the enlargement of individual RGC arbors.[49] $AC1^{-/-}$, $\beta2^{-/-}$, and $AC1^{-/-}$ :: $\beta2^{-/-}$ double-knockout mice show similar retinofugal refinement defects in the first

postnatal week, suggesting an interaction between spontaneous retinal activity and presynaptic AC signaling.[49]

AC/PKA signaling regulates presynaptic release probability in part through the phosphorylation of presynaptic RIM1 proteins.[50–52] RIM zinc finger domains are essential for docking vesicles adjacent to presynaptic Ca^{2+} channels[53] and genetic deletion of RIM1/2 causes eye-specific segregation defects in the dLGN.[54] Similar results have been reported during somatosensory cortical development where thalamocortical synapses in AC1 mutants show defects in presynaptic RIM1 phosphorylation, reduced vesicle release, and abnormal barrel field formation.[51,55] Because AC/PKA signaling has been shown to regulate synaptic vesicle mobility[56] and retention at the AZ,[57] it will be of future interest to investigate eye-specific differences in vesicle pool organization in AC1$^{-/-}$ mutants.

In addition to reduced eye-specific vesicle pool maturation, $\beta2^{-/-}$ mice fail to show an early eye-specific bias in vesicle occupancy at the AZ normally seen in WT mice (Figures 2C–2F). Vesicle number at the AZ is indicative of presynaptic release probability and early eye-specific differences in presynaptic release may induce non-cell-autonomous signaling mechanisms between ipsi- versus contralateral RGC axons.[54,58–63] Genetic deletion of presynaptic VGluT2 or RIM1/2 proteins within a subset of ipsilaterally projecting retinal ganglion cells (RGCs) reduces their presynaptic release probability and prevents the retraction of contralateral fibers from the future ipsilateral termination zone.[54,60] Presynaptic release from co-active inputs may activate synapse elimination signaling pathways (so-called punishment signals) that cause the retraction of uncorrelated (non-dominant-eye) axons. Similar mechanisms have been implicated in synaptic competition between developing neuromuscular axons where a more active motor neuron synapse destabilizes weaker neighboring synapses.[64,65] In the visual system, JAK2 kinase signaling has been implicated as one such punishment signaling pathway and dominant-negative interference with JAK2 signaling in retinogeniculate axons allows non-dominant-eye axons to evade competitive elimination.[62] In addition to punishment signals that destabilize competing eye-specific axons, non-cell-autonomous mechanisms may also help stabilize co-active inputs from the same eye. Downregulation of cAMP signaling in a subset of RGC axons causes neighboring axons from the same eye to develop smaller terminal arbors than controls.[66] This effect is independent of changes in retinal wave activity, suggesting that cAMP signaling mediates a non-cell-autonomous stabilization mechanism in developing retinogeniculate arbors from the same eye of origin.[66]

In addition to biasing neurotransmission efficacy, eye-specific differences in presynaptic vesicle pool development may reflect the selective delivery or capture of proteins that regulate synapse formation versus pruning. Synaptogenesis requires the trafficking and recruitment of synaptic vesicle precursors and AZ proteins which coalesce along developing axons to form presynaptic terminals.[67–69] As synapses mature, they become more active and experience increased vesicle cycling, faster vesicle aging, and increased protein turnover that supports synaptic function.[70–72] Eye-specific differences in the rate of vesicular release may affect the presentation of synaptic tagging molecules that regulate activity-dependent glial phagocytosis of developing synapses.[73,74] Future super-resolution imaging experiments will help evaluate developmentally regulated and eye-specific expression patterns of major histocompatibility complex (MHC) proteins,[75] complement factors,[76] and other immune signaling molecules with important roles in retinogeniculate development.[77]

Changes in SSD organization during eye-specific segregation

In contrast to early eye-specific differences in vesicle organization, we found no eye-specific differences in either active zone (Bassoon) or postsynaptic density (Homer1) SSD number, volume, or signal intensity. Similarly, we observed no eye-specific differences in the alignment of Bassoon and Homer1 SSDs across retinogeniculate synapses in both WT and $\beta2^{-/-}$ mice. Transsynaptic SSD alignment facilitates neurotransmission by bringing independent presynaptic release sites into apposition with receptors and associated PSD proteins.[45] This architecture suggests that changes in SSD number or transsynaptic alignment could impact synaptic strength as a mechanism underlying synaptic competition.[44] Our results, which are consistent with *in vitro* analysis showing activity-independent SSD alignment,[78] suggest that changes in transsynaptic SSD alignment or number do not underlie eye-specific synaptic competition *in vivo*.

Although we found no evidence for eye-specific SSD differences, we did observe both developmental and activity-dependent changes in Homer1 SSD number in retinogeniculate synapses of both eyes. We found that the number of Homer1 SSDs was reduced from P2 to P8 in WT mice while $\beta2^{-/-}$ mice showed an opposite effect (Figures 4B and S4C, bottom panels). Homer1 has been shown to form a matrix at the PSD where it interacts with Shank to help stabilize AMPA and NMDA receptors.[79] Developmental changes in Homer1 SSD organization may reflect PSD maturation that contributes to an increased AMPA/NMDA receptor ratio and the functional unsilencing of retinogeniculate synapses.[3] Consistent with this, functional recording experiments during eye-specific segregation in the superior colliculus (SC) have shown that WT retinocollicular synapses undergo progressive maturation that increases AMPA quantal amplitude, increases the AMPA/NMDA ratio, and decreases the fraction of silent synapses.[80–83] In contrast, $\beta2^{-/-}$ mice show decreased AMPA quantal amplitude, reduced AMPA/NMDA ratio, an increased fraction of silent synapses, and more numerous synaptic connections compared with controls.[80,83]

In contrast to increased retinocollicular synapse density in $\beta2^{-/-}$ mice,[80,83] we found that $\beta2^{-/-}$ mice develop significantly fewer retinogeniculate synapses from both eyes compared with WT controls. Such regional differences in synaptic development could arise from the unique expression of different Ca^{2+} channel types in dLGN versus SC retinofugal terminals which may differentially affect presynaptic Ca^{2+} levels and related downstream signaling.[84] Region-specific differences in presynaptic AZ composition may also contribute as evidenced by the finding that genetic deletion of RIM1/2 proteins from RGC terminals disrupts eye-specific refinement in the dLGN with no impact on eye-specific segregation in the SC.[54] Considering that the majority of retinal ganglion cells project to both the dLGN and

SC,[85] it will be of interest to further characterize region-specific differences in the ultrastructural development of synaptic inputs from distinct RGC types.[86] Additionally, future functional recording experiments during eye-specific segregation in the dLGN will be informative for comparison with previously published results in the SC.

The relationship between synapse development and axon refinement

The activity-dependent defects we measured in eye-specific synaptogenesis and presynaptic terminal development offer further support for a synaptotropic hypothesis of neurite development in which the accumulation/stabilization of presynaptic proteins regulates the formation and stability of neurite branches.[87] Live imaging of developing frog retinotectal axon dynamics has shown that vesicle accumulation over time stabilizes presynaptic terminals and local axon branching near synaptic sites.[88] Branch stabilization requires presynaptic release and experiments to genetically silence individual axons result in exuberant branching phenotypes.[58] In addition, targeted axon branching is regulated by RGC activity following a Hebbian plasticity rule where correlated activity among neighboring RGCs stabilizes axon branches while uncorrelated activity increases axon branching dynamics[89,90] through a non-cell-autonomous signal.[61]

In contrast to live imaging, static STORM images cannot resolve fast dynamics of synaptic turnover that may occur in axons of both eyes during competition. However, STORM snapshots revealed developmental changes in eye-specific synapse density and presynaptic size which suggest the formation/maintenance of stable synapses in future eye-specific territories. Dominant-eye synapse density increased over development and was driven by an increase in synapses with larger presynaptic vesicle pools. In contrast, non-dominant-eye synapse density decreased over development and smaller synapses were lost at a greater rate. Together, these results suggest that differences in eye-specific synapse stability underlie eye-specific branching patterns. Compared with WT, $\beta2^{-/-}$ mice have disrupted cholinergic wave properties that reduce the precision of correlated RGC input to the dLGN[24,25] and result in an enlargement of individual retinogeniculate axon arbors.[21] In this context, our finding that $\beta2^{-/-}$ mice have significantly fewer synapses and disrupted presynaptic vesicle pool organization compared with WT controls is consistent with the hypothesis that synapse formation/stabilization is an important regulator of local axon branching. Future high-resolution imaging experiments combining synaptic and axonal labeling will be useful to explore relationships between synaptic turnover and neurite branching during retinogeniculate circuit development.

Limitations of the study

The data presented in this study are snapshots of development taken from ROIs selected in the dLGN core for comparison across ages and genotypes. However, the rodent dLGN is known to exhibit regional differences in retinal input, particularly between core and shell domains, and these may undergo different patterns of synaptic refinement during development that were not captured in the current study.[91,92] Furthermore, our synaptic images using CTB for eye-specific labeling do not provide information on the RGC type identities of individual retinogeniculate synapses. Because diverse RGC types converge to form synaptic glomeruli on individual relay neuron branches,[93–95] it will be informative to use RGC type-specific transgenic labeling in future super-resolution studies to investigate the development of synaptic connections conveying unique visual representations to the brain.

The combination of single-molecule localization microscopy and sample ultrasectioning that we used to achieve volumetric STORM reconstructions requires technical skill and sacrifices imaging speed for increased spatial resolution.[36] However, because the sample preparation method is similar to serial-section EM, there is future potential to integrate super-resolution light and EM to achieve dense connectomic reconstructions together with molecular-specific information at individual synaptic connections and cellular contacts.[96,97] Similar to EM, STORM images reveal static synaptic features. By comparing eye-specific synapses at different ages, we showed the association of specific subsynaptic properties (particularly vesicle organization) with the future outcome of eye-specific competition (Figures 2 and 3). A more complete understanding of how specific morphological features drive synaptic competition will require new experiments with higher temporal resolution necessary to resolve dynamic changes in developing synapses *in vivo*.

We performed the current experiments using four spectrally separate color channels, which limited our ability to interrogate a large number of known synaptic and signaling proteins with important roles in eye-specific segregation. In the future, multiplexed labeling approaches could help increase the number of protein species imaged within individual samples and enable network analyses of synaptic remodeling during activity-dependent development.[98,99] Finally, the spatial resolution of our approach is currently limited by a combination of the localization precision of the fluorophores used (~18–30 nm),[100] the labeling density and linkage error associated with indirect immunohistochemistry (~20 nm),[101] and the physical thickness (Z dimension) of our ultrathin sections (70 nm).[36] Theoretical and technical advances that increase the spatial resolution of super-resolution microscopy[102,103] will have immediate applications to the imaging of serial-section arrays, leading us closer to molecular scale analysis of synaptic protein assemblies *in situ*.

STAR★METHODS

Detailed methods are provided in the online version of this paper and include the following:

- KEY RESOURCES TABLE
- RESOURCE AVAILABILITY
  - Lead contact
  - Materials availability
  - Data and code availability
- EXPERIMENTAL MODEL AND SUBJECT DETAILS
  - Animals
- METHOD DETAILS
  - Eye injections
  - dLGN tissue preparation

- Immunohistochemistry
- Postfixation, dehydration, and embedding in epoxy resin
- Ultrasectioning
- Imaging chamber preparation
- Imaging setup
- Automated image acquisition
- Image processing
- Cell body filter
- Eye-specific synapse identification and quantification
- VGluT2 population analysis
- Analysis of vesicles associated with the AZ
- SSD analysis based on voxel intensity distributions
- SSD analysis based on single molecule localization distributions

- QUANTIFICATION AND STATISTICAL ANALYSIS

SUPPLEMENTAL INFORMATION

Supplemental information can be found online at https://doi.org/10.1016/j.celrep.2023.112085.

ACKNOWLEDGMENTS

We thank Dr. Michael C. Crair for generously sharing the $\beta2^{-/-}$ mouse line used in this work. We also thank the statistical consulting program at the UMD Libraries for advice concerning statistical analyses. We are grateful to Jacqueline A. Minehart and Rashmi Gupta for creative feedback on the graphical abstract. The research was funded by National Institutes of Health grant DP2MH125812 (C.M.S.) and institutional startup support provided by the University of Maryland.

AUTHOR CONTRIBUTIONS

Conceptualization, C.Z. and C.M.S.; data curation, C.Z., S.Y., and C.M.S.; formal analysis, C.Z., S.Y., and C.M.S.; funding acquisition, C.M.S.; investigation, C.Z. and C.M.S.; methodology, C.Z., S.Y., and C.M.S.; project administration, C.Z. and C.M.S.; resources, C.Z. and C.M.S.; software, C.Z., S.Y., and C.M.S.; supervision, C.M.S.; validation, C.Z. and C.M.S.; visualization, C.Z. and C.M.S.; writing – original draft preparation, C.Z. and C.M.S.; writing – review & editing, C.Z., S.Y., and C.M.S.

DECLARATION OF INTERESTS

The authors declare no competing interests.

INCLUSION AND DIVERSITY

We worked to ensure sex balance in the selection of non-human subjects. We support inclusive, diverse, and equitable conduct of research.

Received: May 31, 2022
Revised: December 23, 2022
Accepted: January 24, 2023

REFERENCES

1. Guido, W. (2018). Development, form, and function of the mouse visual thalamus. J. Neurophysiol. *120*, 211–225. https://doi.org/10.1152/jn.00651.2017.
2. Kirkby, L.A., Sack, G.S., Firl, A., and Feller, M.B. (2013). A role for correlated spontaneous activity in the assembly of neural circuits. Neuron *80*, 1129–1144. https://doi.org/10.1016/j.neuron.2013.10.030.
3. Litvina, E.Y., and Chen, C. (2017). An evolving view of retinogeniculate transmission. Vis. Neurosci. *34*, E013. https://doi.org/10.1017/S0952523817000104.
4. Shatz, C.J. (1990). Competitive interactions between retinal ganglion cells during prenatal development. J. Neurobiol. *21*, 197–211. https://doi.org/10.1002/neu.480210113.
5. Godement, P., Salaün, J., and Imbert, M. (1984). Prenatal and postnatal development of retinogeniculate and retinocollicular projections in the mouse. J. Comp. Neurol. *230*, 552–575. https://doi.org/10.1002/cne.902300406.
6. Ackman, J.B., and Crair, M.C. (2014). Role of emergent neural activity in visual map development. Curr. Opin. Neurobiol. *24*, 166–175. https://doi.org/10.1016/j.conb.2013.11.011.
7. Arroyo, D.A., and Feller, M.B. (2016). Spatiotemporal features of retinal waves instruct the wiring of the visual circuitry. Front. Neural Circ. *10*, 54. https://doi.org/10.3389/fncir.2016.00054.
8. Blank, M., Fuerst, P.G., Stevens, B., Nouri, N., Kirkby, L., Warrier, D., Barres, B.A., Feller, M.B., Huberman, A.D., Burgess, R.W., and Garner, C.C. (2011). The Down syndrome critical region regulates retinogeniculate refinement. J. Neurosci. *31*, 5764–5776. https://doi.org/10.1523/JNEUROSCI.6015-10.2011.
9. Cook, P.M., Prusky, G., and Ramoa, A.S. (1999). The role of spontaneous retinal activity before eye opening in the maturation of form and function in the retinogeniculate pathway of the ferret. Vis. Neurosci. *16*, 491–501. https://doi.org/10.1017/S0952523899163107.
10. Failor, S., Chapman, B., and Cheng, H.J. (2015). Retinal waves regulate afferent terminal targeting in the early visual pathway. Proc. Natl. Acad. Sci. USA *112*, E2957–E2966. https://doi.org/10.1073/pnas.1506458112.
11. Huberman, A.D., Stellwagen, D., and Chapman, B. (2002). Decoupling eye-specific segregation from lamination in the lateral geniculate nucleus. J. Neurosci. *22*, 9419–9429. https://doi.org/10.1523/JNEUROSCI.22-21-09419.2002.
12. Huberman, A.D., Wang, G.-Y., Liets, L.C., Collins, O.A., Chapman, B., and Chalupa, L.M. (2003). Eye-specific retinogeniculate segregation independent of normal neuronal activity. Science *300*, 994–998. https://doi.org/10.1126/science.1080694.
13. Penn, A.A., Riquelme, P.A., Feller, M.B., and Shatz, C.J. (1998). Competition in retinogeniculate patterning driven by spontaneous activity. Science *279*, 2108–2112. https://doi.org/10.1126/science.279.5359.2108.
14. Pfeiffenberger, C., Cutforth, T., Woods, G., Yamada, J., Rentería, R.C., Copenhagen, D.R., Flanagan, J.G., and Feldheim, D.A. (2005). Ephrin-As and neural activity are required for eye-specific patterning during retinogeniculate mapping. Nat. Neurosci. *8*, 1022–1027. https://doi.org/10.1038/nn1508.
15. Rebsam, A., Petros, T.J., and Mason, C.A. (2009). Switching retinogeniculate axon laterality leads to normal targeting but abnormal eye-specific segregation that is activity dependent. J. Neurosci. *29*, 14855–14863. https://doi.org/10.1523/JNEUROSCI.3462-09.2009.
16. Rebsam, A., Bhansali, P., and Mason, C.A. (2012). Eye-specific projections of retinogeniculate axons are altered in albino mice. J. Neurosci. *32*, 4821–4826. https://doi.org/10.1523/JNEUROSCI.5050-11.2012.
17. Rossi, F.M., Pizzorusso, T., Porciatti, V., Marubio, L.M., Maffei, L., and Changeux, J.P. (2001). Requirement of the nicotinic acetylcholine receptor beta 2 subunit for the anatomical and functional development of the visual system. Proc. Natl. Acad. Sci. USA *98*, 6453–6458. https://doi.org/10.1073/pnas.101120998.
18. Shatz, C.J., and Stryker, M.P. (1988). Prenatal tetrodotoxin infusion blocks segregation of retinogeniculate afferents. Science *242*, 87–89. https://doi.org/10.1126/science.3175636.
19. Speer, C.M., Sun, C., Liets, L.C., Stafford, B.K., Chapman, B., and Cheng, H.J. (2014). Eye-specific retinogeniculate segregation proceeds normally following disruption of patterned spontaneous retinal activity. Neural Dev. *9*, 25. https://doi.org/10.1186/1749-8104-9-25.

20. Stellwagen, D., and Shatz, C.J. (2002). An instructive role for retinal waves in the development of retinogeniculate connectivity. Neuron *33*, 357–367. https://doi.org/10.1016/s0896-6273(02)00577-9.

21. Dhande, O.S., Hua, E.W., Guh, E., Yeh, J., Bhatt, S., Zhang, Y., Ruthazer, E.S., Feller, M.B., and Crair, M.C. (2011). Development of single retinofugal axon arbors in normal and beta2 knock-out mice. J. Neurosci. *31*, 3384–3399. https://doi.org/10.1523/JNEUROSCI.4899-10.2011.

22. Grubb, M.S., Rossi, F.M., Changeux, J.P., and Thompson, I.D. (2003). Abnormal functional organization in the dorsal lateral geniculate nucleus of mice lacking the beta 2 subunit of the nicotinic acetylcholine receptor. Neuron *40*, 1161–1172. https://doi.org/10.1016/s0896-6273(03)00789-x.

23. Muir-Robinson, G., Hwang, B.J., and Feller, M.B. (2002). Retinogeniculate axons undergo eye-specific segregation in the absence of eye-specific layers. J. Neurosci. *22*, 5259–5264. https://doi.org/10.1523/JNEUROSCI.22-13-05259.

24. Stafford, B.K., Sher, A., Litke, A.M., and Feldheim, D.A. (2009). Spatial-temporal patterns of retinal waves underlying activity-dependent refinement of retinofugal projections. Neuron *64*, 200–212. https://doi.org/10.1016/j.neuron.2009.09.021.

25. Sun, C., Warland, D.K., Ballesteros, J.M., van der List, D., and Chalupa, L.M. (2008). Retinal waves in mice lacking the beta2 subunit of the nicotinic acetylcholine receptor. Proc. Natl. Acad. Sci. USA *105*, 13638–13643. https://doi.org/10.1073/pnas.0807178105.

26. Xu, H.P., Burbridge, T.J., Chen, M.G., Ge, X., Zhang, Y., Zhou, Z.J., and Crair, M.C. (2015). Spatial pattern of spontaneous retinal waves instructs retinotopic map refinement more than activity frequency. Dev. Neurobiol. *75*, 621–640. https://doi.org/10.1002/dneu.22288.

27. Xu, H.P., Burbridge, T.J., Ye, M., Chen, M., Ge, X., Zhou, Z.J., and Crair, M.C. (2016). Retinal wave patterns are governed by mutual excitation among starburst amacrine cells and drive the refinement and maintenance of visual circuits. J. Neurosci. *36*, 3871–3886. https://doi.org/10.1523/JNEUROSCI.3549-15.2016.

28. Xu, H.P., Furman, M., Mineur, Y.S., Chen, H., King, S.L., Zenisek, D., Zhou, Z.J., Butts, D.A., Tian, N., Picciotto, M.R., and Crair, M.C. (2011). An instructive role for patterned spontaneous retinal activity in mouse visual map development. Neuron *70*, 1115–1127. https://doi.org/10.1016/j.neuron.2011.04.028.

29. Campbell, G., and Shatz, C.J. (1992). Synapses formed by identified retinogeniculate axons during the segregation of eye input. J. Neurosci. *12*, 1847–1858.

30. Sretavan, D., and Shatz, C.J. (1984). Prenatal development of individual retinogeniculate axons during the period of segregation. Nature *308*, 845–848. https://doi.org/10.1038/308845a0.

31. Sretavan, D.W., and Shatz, C.J. (1987). Axon trajectories and pattern of terminal arborization during the prenatal development of the cat's retinogeniculate pathway. J. Comp. Neurol. *255*, 386–400. https://doi.org/10.1002/cne.902550306.

32. Sretavan, D.W., and Shatz, C.J. (1986). Prenatal development of cat retinogeniculate axon arbors in the absence of binocular interactions. J. Neurosci. *6*, 990–1003.

33. Sretavan, D.W., and Shatz, C.J. (1986). Prenatal development of retinal ganglion cell axons: segregation into eye-specific layers within the cat's lateral geniculate nucleus. J. Neurosci. *6*, 234–251.

34. Bickford, M.E., Slusarczyk, A., Dilger, E.K., Krahe, T.E., Kucuk, C., and Guido, W. (2010). Synaptic development of the mouse dorsal lateral geniculate nucleus. J. Comp. Neurol. *518*, 622–635. https://doi.org/10.1002/cne.22223.

35. Sigal, Y.M., Speer, C.M., Babcock, H.P., and Zhuang, X. (2015). Mapping synaptic input fields of neurons with super-resolution imaging. Cell *163*, 493–505. https://doi.org/10.1016/j.cell.2015.08.033.

36. Vatan, T., Minehart, J.A., Zhang, C., Agarwal, V., Yang, J., and Speer, C.M. (2021). Volumetric super-resolution imaging by serial ultrasectioning and stochastic optical reconstruction microscopy in mouse neural tissue. STAR Protoc. *2*, 100971. https://doi.org/10.1016/j.xpro.2021.100971.

37. El-Danaf, R.N., Krahe, T.E., Dilger, E.K., Bickford, M.E., Fox, M.A., and Guido, W. (2015). Developmental remodeling of relay cells in the dorsal lateral geniculate nucleus in the absence of retinal input. Neural Dev. *10*, 19. https://doi.org/10.1186/s13064-015-0046-6.

38. Fujiyama, F., Hioki, H., Tomioka, R., Taki, K., Tamamaki, N., Nomura, S., Okamoto, K., and Kaneko, T. (2003). Changes of immunocytochemical localization of vesicular glutamate transporters in the rat visual system after the retinofugal denervation. J. Comp. Neurol. *465*, 234–249. https://doi.org/10.1002/cne.10848.

39. Hammer, S., Carrillo, G.L., Govindaiah, G., Monavarfeshani, A., Bircher, J.S., Su, J., Guido, W., and Fox, M.A. (2014). Nuclei-specific differences in nerve terminal distribution, morphology, and development in mouse visual thalamus. Neural Dev. *9*, 16. https://doi.org/10.1186/1749-8104-9-16.

40. Land, P.W., Kyonka, E., and Shamalla-Hannah, L. (2004). Vesicular glutamate transporters in the lateral geniculate nucleus: expression of VGLUT2 by retinal terminals. Brain Res. *996*, 251–254. https://doi.org/10.1016/j.brainres.2003.10.032.

41. Grubb, M.S., and Thompson, I.D. (2004). Biochemical and anatomical subdivision of the dorsal lateral geniculate nucleus in normal mice and in mice lacking the beta2 subunit of the nicotinic acetylcholine receptor. Vis. Res. *44*, 3365–3376. https://doi.org/10.1016/j.visres.2004.09.003.

42. Kaeser, P.S., and Regehr, W.G. (2017). The readily releasable pool of synaptic vesicles. Curr. Opin. Neurobiol. *43*, 63–70. https://doi.org/10.1016/j.conb.2016.12.012.

43. Voronin, L.L., and Cherubini, E. (2004). 'Deaf, mute and whispering' silent synapses: their role in synaptic plasticity. J. Physiol. *557*, 3–12. https://doi.org/10.1113/jphysiol.2003.058966.

44. Chen, H., Tang, A.H., and Blanpied, T.A. (2018). Subsynaptic spatial organization as a regulator of synaptic strength and plasticity. Curr. Opin. Neurobiol. *51*, 147–153. https://doi.org/10.1016/j.conb.2018.05.004.

45. Tang, A.H., Chen, H., Li, T.P., Metzbower, S.R., MacGillavry, H.D., and Blanpied, T.A. (2016). A trans-synaptic nanocolumn aligns neurotransmitter release to receptors. Nature *536*, 210–214. https://doi.org/10.1038/nature19058.

46. Fassier, C., and Nicol, X. (2021). Retinal axon interplay for binocular mapping. Front. Neural Circ. *15*, 679440. https://doi.org/10.3389/fncir.2021.679440.

47. Nicol, X., Bennis, M., Ishikawa, Y., Chan, G.C.K., Repérant, J., Storm, D.R., and Gaspar, P. (2006). Role of the calcium modulated cyclases in the development of the retinal projections. Eur. J. Neurosci. *24*, 3401–3414. https://doi.org/10.1111/j.1460-9568.2006.05227.x.

48. Ravary, A., Muzerelle, A., Hervé, D., Pascoli, V., Ba-Charvet, K.N., Girault, J.-A., Welker, E., and Gaspar, P. (2003). Adenylate cyclase 1 as a key actor in the refinement of retinal projection maps. J. Neurosci. *23*, 2228–2238. https://doi.org/10.1523/JNEUROSCI.23-06-02228.

49. Dhande, O.S., Bhatt, S., Anishchenko, A., Elstrott, J., Iwasato, T., Swindell, E.C., Xu, H.P., Jamrich, M., Itohara, S., Feller, M.B., and Crair, M.C. (2012). Role of adenylate cyclase 1 in retinofugal map development. J. Comp. Neurol. *520*, 1562–1583. https://doi.org/10.1002/cne.23000.

50. Kohansal-Nodehi, M., Chua, J.J., Urlaub, H., Jahn, R., and Czernik, D. (2016). Analysis of protein phosphorylation in nerve terminal reveals extensive changes in active zone proteins upon exocytosis. Elife *5*, e14530. https://doi.org/10.7554/eLife.14530.

51. Lu, H.C., Butts, D.A., Kaeser, P.S., She, W.C., Janz, R., and Crair, M.C. (2006). Role of efficient neurotransmitter release in barrel map development. J. Neurosci. *26*, 2692–2703. https://doi.org/10.1523/JNEUROSCI.3956-05.2006.

52. Müller, J.A., Betzin, J., Santos-Tejedor, J., Mayer, A., Oprişoreanu, A.M., Engholm-Keller, K., Paulußen, I., Gulakova, P., McGovern, T.D.,

Gschossman, L.J., et al. (2022). A presynaptic phosphosignaling hub for lasting homeostatic plasticity. Cell Rep. *39*, 110696. https://doi.org/10.1016/j.celrep.2022.110696.

53. Tan, C., Wang, S.S.H., de Nola, G., and Kaeser, P.S. (2022). Rebuilding essential active zone functions within a synapse. Neuron *110*, 1498–1515.e8. https://doi.org/10.1016/j.neuron.2022.01.026.
54. Assali, A., Le Magueresse, C., Bennis, M., Nicol, X., Gaspar, P., and Rebsam, A. (2017). RIM1/2 in retinal ganglion cells are required for the refinement of ipsilateral axons and eye-specific segregation. Sci. Rep. *7*, 3236. https://doi.org/10.1038/s41598-017-03361-0.
55. Suzuki, A., Lee, L.J., Hayashi, Y., Muglia, L., Itohara, S., Erzurumlu, R.S., and Iwasato, T. (2015). Thalamic adenylyl cyclase 1 is required for barrel formation in the somatosensory cortex. Neuroscience *290*, 518–529. https://doi.org/10.1016/j.neuroscience.2015.01.043.
56. Chenouard, N., Xuan, F., and Tsien, R.W. (2020). Synaptic vesicle traffic is supported by transient actin filaments and regulated by PKA and NO. Nat. Commun. *11*, 5318. https://doi.org/10.1038/s41467-020-19120-1.
57. Rey, S., Marra, V., Smith, C., and Staras, K. (2020). Nanoscale remodeling of functional synaptic vesicle pools in hebbian plasticity. Cell Rep. *30*, 2006–2017.e3. https://doi.org/10.1016/j.celrep.2020.01.051.
58. Ben Fredj, N., Hammond, S., Otsuna, H., Chien, C.B., Burrone, J., and Meyer, M.P. (2010). Synaptic activity and activity-dependent competition regulates axon arbor maturation, growth arrest, and territory in the retinotectal projection. J. Neurosci. *30*, 10939–10951. https://doi.org/10.1523/JNEUROSCI.1556-10.2010.
59. Hua, J.Y., Smear, M.C., Baier, H., and Smith, S.J. (2005). Regulation of axon growth in vivo by activity-based competition. Nature *434*, 1022–1026. https://doi.org/10.1038/nature03409.
60. Koch, S.M., Dela Cruz, C.G., Hnasko, T.S., Edwards, R.H., Huberman, A.D., and Ullian, E.M. (2011). Pathway-specific genetic attenuation of glutamate release alters select features of competition-based visual circuit refinement. Neuron *71*, 235–242. https://doi.org/10.1016/j.neuron.2011.05.045.
61. Rahman, T.N., Munz, M., Kutsarova, E., Bilash, O.M., and Ruthazer, E.S. (2020). Stentian structural plasticity in the developing visual system. Proc. Natl. Acad. Sci. USA *117*, 10636–10638. https://doi.org/10.1073/pnas.2001107117.
62. Yasuda, M., Nagappan-Chettiar, S., Johnson-Venkatesh, E.M., and Umemori, H. (2021). An activity-dependent determinant of synapse elimination in the mammalian brain. Neuron *109*, 1333–1349.e6. https://doi.org/10.1016/j.neuron.2021.03.006.
63. Zhang, L.I., Tao, H.W., Holt, C.E., Harris, W.A., and Poo, M. (1998). A critical window for cooperation and competition among developing retinotectal synapses. Nature *395*, 37–44. https://doi.org/10.1038/25665.
64. Balice-Gordon, R.J., and Lichtman, J.W. (1994). Long-term synapse loss induced by focal blockade of postsynaptlc receptors. Nature *372*, 519–524. https://doi.org/10.1038/372519a0.
65. Buffelli, M., Burgess, R.W., Feng, G., Lobe, C.G., Lichtman, J.W., and Sanes, J.R. (2003). Genetic evidence that relative synaptic efficacy biases the outcome of synaptic competition. Nature *424*, 430–434. https://doi.org/10.1038/nature01844.
66. Louail, A., Sierksma, M.C., Chaffiol, A., Baudet, S., Assali, A., Couvet, S., Nedjam, M., Roche, F., Zagar, Y., Duebel, J., and Nicol, X. (2020). cAMP-dependent Co-stabilization of axonal arbors from adjacent developing neurons. Cell Rep. *33*, 108220. https://doi.org/10.1016/j.celrep.2020.108220.
67. Bury, L.A.D., and Sabo, S.L. (2016). Building a terminal: mechanisms of presynaptic development in the CNS. Neuroscientist *22*, 372–391. https://doi.org/10.1177/1073858415596131.
68. Guedes-Dias, P., and Holzbaur, E.L.F. (2019). Axonal transport: driving synaptic function. Science *366*, eaaw9997. https://doi.org/10.1126/science.aaw9997.
69. Rizalar, F.S., Roosen, D.A., and Haucke, V. (2021). A presynaptic perspective on transport and assembly mechanisms for synapse formation. Neuron *109*, 27–41. https://doi.org/10.1016/j.neuron.2020.09.038.
70. Denker, A., Kröhnert, K., Bückers, J., Neher, E., and Rizzoli, S.O. (2011). The reserve pool of synaptic vesicles acts as a buffer for proteins involved in synaptic vesicle recycling. Proc. Natl. Acad. Sci. USA *108*, 17183–17188. https://doi.org/10.1073/pnas.1112690108.
71. Jähne, S., Mikulasch, F., Heuer, H.G.H., Truckenbrodt, S., Agüi-Gonzalez, P., Grewe, K., Vogts, A., Rizzoli, S.O., and Priesemann, V. (2021). Presynaptic activity and protein turnover are correlated at the single-synapse level. Cell Rep. *34*, 108841. https://doi.org/10.1016/j.celrep.2021.108841.
72. Truckenbrodt, S., Viplav, A., Jähne, S., Vogts, A., Denker, A., Wildhagen, H., Fornasiero, E.F., and Rizzoli, S.O. (2018). Newly produced synaptic vesicle proteins are preferentially used in synaptic transmission. EMBO J. *37*, e98044. https://doi.org/10.15252/embj.201798044.
73. Cong, Q., Soteros, B.M., Wollet, M., Kim, J.H., and Sia, G.M. (2020). The endogenous neuronal complement inhibitor SRPX2 protects against complement-mediated synapse elimination during development. Nat. Neurosci. *23*, 1067–1078. https://doi.org/10.1038/s41593-020-0672-0.
74. Wilton, D.K., Dissing-Olesen, L., and Stevens, B. (2019). Neuron-glia signaling in synapse elimination. Annu. Rev. Neurosci. *42*, 107–127. https://doi.org/10.1146/annurev-neuro-070918-050306.
75. Datwani, A., McConnell, M.J., Kanold, P.O., Micheva, K.D., Busse, B., Shamloo, M., Smith, S.J., and Shatz, C.J. (2009). Classical MHCI molecules regulate retinogeniculate refinement and limit ocular dominance plasticity. Neuron *64*, 463–470. https://doi.org/10.1016/j.neuron.2009.10.015.
76. Schafer, D.P., Lehrman, E.K., Kautzman, A.G., Koyama, R., Mardinly, A.R., Yamasaki, R., Ransohoff, R.M., Greenberg, M.E., Barres, B.A., and Stevens, B. (2012). Microglia sculpt postnatal neural circuits in an activity and complement-dependent manner. Neuron *74*, 691–705. https://doi.org/10.1016/j.neuron.2012.03.026.
77. Faust, T.E., Gunner, G., and Schafer, D.P. (2021). Mechanisms governing activity-dependent synaptic pruning in the developing mammalian CNS. Nat. Rev. Neurosci. *22*, 657–673. https://doi.org/10.1038/s41583-021-00507-y.
78. Sun, S.Y., Li, X.W., Cao, R., Zhao, Y., Sheng, N., and Tang, A.H. (2022). Correlative assembly of subsynaptic nanoscale organizations during development. Front. Synaptic Neurosci. *14*, 748184. https://doi.org/10.3389/fnsyn.2022.748184.
79. Hayashi, M.K., Tang, C., Verpelli, C., Narayanan, R., Stearns, M.H., Xu, R.M., Li, H., Sala, C., and Hayashi, Y. (2009). The postsynaptic density proteins Homer and Shank form a polymeric network structure. Cell *137*, 159–171. https://doi.org/10.1016/j.cell.2009.01.050.
80. Chandrasekaran, A.R., Shah, R.D., and Crair, M.C. (2007). Developmental homeostasis of mouse retinocollicular synapses. J. Neurosci. *27*, 1746–1755. https://doi.org/10.1523/JNEUROSCI.4383-06.2007.
81. Furman, M., and Crair, M.C. (2012). Synapse maturation is enhanced in the binocular region of the retinocollicular map prior to eye opening. J. Neurophysiol. *107*, 3200–3216. https://doi.org/10.1152/jn.00943.2011.
82. Furman, M., Xu, H.P., and Crair, M.C. (2013). Competition driven by retinal waves promotes morphological and functional synaptic development of neurons in the superior colliculus. J. Neurophysiol. *110*, 1441–1454. https://doi.org/10.1152/jn.01066.2012.
83. Shah, R.D., and Crair, M.C. (2008). Retinocollicular synapse maturation and plasticity are regulated by correlated retinal waves. J. Neurosci. *28*, 292–303. https://doi.org/10.1523/JNEUROSCI.4276-07.2008.
84. Govindaiah, G., Campbell, P.W., and Guido, W. (2020). Differential distribution of Ca(2+) channel subtypes at retinofugal synapses. eNeuro *7*, ENEURO.0293–20.2020. https://doi.org/10.1523/ENEURO.0293-20.2020.

85. Ellis, E.M., Gauvain, G., Sivyer, B., and Murphy, G.J. (2016). Shared and distinct retinal input to the mouse superior colliculus and dorsal lateral geniculate nucleus. J. Neurophysiol. *116*, 602–610. https://doi.org/10.1152/jn.00227.2016.

86. Kim, K.Y., Rios, L.C., Le, H., Perez, A.J., Phan, S., Bushong, E.A., Deerinck, T.J., Liu, Y.H., Ellisman, M.A., Lev-Ram, V., et al. (2019). Synaptic specializations of melanopsin-retinal ganglion cells in multiple brain regions revealed by genetic label for light and electron microscopy. Cell Rep. *29*, 628–644.e6. https://doi.org/10.1016/j.celrep.2019.09.006.

87. Vaughn, J.E. (1989). Fine structure of synaptogenesis in the vertebrate central nervous system. Synapse *3*, 255–285. https://doi.org/10.1002/syn.890030312.

88. Ruthazer, E.S., Li, J., and Cline, H.T. (2006). Stabilization of axon branch dynamics by synaptic maturation. J. Neurosci. *26*, 3594–3603. https://doi.org/10.1523/JNEUROSCI.0069-06.2006.

89. Munz, M., Gobert, D., Schohl, A., Poquérusse, J., Podgorski, K., Spratt, P., and Ruthazer, E.S. (2014). Rapid Hebbian axonal remodeling mediated by visual stimulation. Science *344*, 904–909. https://doi.org/10.1126/science.1251593.

90. Ruthazer, E.S., Akerman, C.J., and Cline, H.T. (2003). Control of axon branch dynamics by correlated activity in vivo. Science *301*, 66–70. https://doi.org/10.1126/science.1082545.

91. Kerschensteiner, D., and Guido, W. (2017). Organization of the dorsal lateral geniculate nucleus in the mouse. Vis. Neurosci. *34*, E008. https://doi.org/10.1017/S0952523817000062.

92. Reese, B.E. (1988). 'Hidden lamination' in the dorsal lateral geniculate nucleus: the functional organization of this thalamic region in the rat. Brain Res. *472*, 119–137. https://doi.org/10.1016/0165-0173(88)90017-3.

93. Hammer, S., Monavarfeshani, A., Lemon, T., Su, J., and Fox, M.A. (2015). Multiple retinal axons converge onto relay cells in the adult mouse thalamus. Cell Rep. *12*, 1575–1583. https://doi.org/10.1016/j.celrep.2015.08.003.

94. Liang, L., Fratzl, A., Goldey, G., Ramesh, R.N., Sugden, A.U., Morgan, J.L., Chen, C., and Andermann, M.L. (2018). A fine-scale functional logic to convergence from retina to thalamus. Cell *173*, 1343–1355.e24. https://doi.org/10.1016/j.cell.2018.04.041.

95. Morgan, J.L., Berger, D.R., Wetzel, A.W., and Lichtman, J.W. (2016). The fuzzy logic of network connectivity in mouse visual thalamus. Cell *165*, 192–206. https://doi.org/10.1016/j.cell.2016.02.033.

96. de Boer, P., Hoogenboom, J.P., and Giepmans, B.N.G. (2015). Correlated light and electron microscopy: ultrastructure lights up. Nat. Methods *12*, 503–513. https://doi.org/10.1038/nmeth.3400.

97. Heiligenstein, X., and Lucas, M.S. (2022). One for all, all for one: a close look at in-resin fluorescence protocols for CLEM. Front. Cell Dev. Biol. *10*, 866472. https://doi.org/10.3389/fcell.2022.866472.

98. Minehart, J.A., and Speer, C.M. (2020). A picture worth a thousand molecules-integrative technologies for mapping subcellular molecular organization and plasticity in developing circuits. Front. Synaptic Neurosci. *12*, 615059. https://doi.org/10.3389/fnsyn.2020.615059.

99. Schueder, F., Unterauer, E.M., Ganji, M., and Jungmann, R. (2020). DNA-barcoded fluorescence microscopy for spatial omics. Proteomics *20*, e1900368. https://doi.org/10.1002/pmic.201900368.

100. Dempsey, G.T., Vaughan, J.C., Chen, K.H., Bates, M., and Zhuang, X. (2011). Evaluation of fluorophores for optimal performance in localization-based super-resolution imaging. Nat. Methods *8*, 1027–1036. https://doi.org/10.1038/nmeth.1768.

101. Lelek, M., Gyparaki, M.T., Beliu, G., Schueder, F., Griffié, J., Manley, S., Jungmann, R., Sauer, M., Lakadamyali, M., and Zimmer, C. (2021). Single-molecule localization microscopy. Nat. Rev. Methods Primers *1*, 39. https://doi.org/10.1038/s43586-021-00038-x.

102. Dankovich, T.M., and Rizzoli, S.O. (2021). Challenges facing quantitative large-scale optical super-resolution, and some simple solutions. iScience *24*, 102134. https://doi.org/10.1016/j.isci.2021.102134.

103. Liu, S., Hoess, P., and Ries, J. (2022). Super-resolution microscopy for structural cell biology. Annu. Rev. Biophys. *51*, 301–326. https://doi.org/10.1146/annurev-biophys-102521-112912.

104. Burbridge, T.J., Xu, H.P., Ackman, J.B., Ge, X., Zhang, Y., Ye, M.J., Zhou, Z.J., Xu, J., Contractor, A., and Crair, M.C. (2014). Visual circuit development requires patterned activity mediated by retinal acetylcholine receptors. Neuron *84*, 1049–1064. https://doi.org/10.1016/j.neuron.2014.10.051.

105. Babcock, H., Sigal, Y.M., and Zhuang, X. (2012). A high-density 3D localization algorithm for stochastic optical reconstruction microscopy. Opt. Nanoscopy *1*, 6. https://doi.org/10.1186/2192-2853-1-6.

106. Schindelin, J., Arganda-Carreras, I., Frise, E., Kaynig, V., Longair, M., Pietzsch, T., Preibisch, S., Rueden, C., Saalfeld, S., Schmid, B., et al. (2012). Fiji: an open-source platform for biological-image analysis. Nat. Methods *9*, 676–682. https://doi.org/10.1038/nmeth.2019.

107. Picciotto, M.R., Zoli, M., Léna, C., Bessis, A., Lallemand, Y., Le Novère, N., Vincent, P., Pich, E.M., Brûlet, P., and Changeux, J.P. (1995). Abnormal avoidance learning in mice lacking functional high-affinity nicotine receptor in the brain. Nature *374*, 65–67. https://doi.org/10.1038/374065a0.

STAR★METHODS

KEY RESOURCES TABLE

REAGENT or RESOURCE	SOURCE	IDENTIFIER
Antibodies		
Donkey anti-Guinea pig IgG unconjugated (1:100)	Jackson ImmunoResearch	Cat#706-005-148; RRID: AB_2340443
Donkey anti-Mouse IgG unconjugated (1:100)	Jackson ImmunoResearch	Cat#715-005-150; RRID: AB_2340758
Donkey anti-Rabbit IgG unconjugated (1:100)	Jackson ImmunoResearch	Cat#711-005-152; RRID: AB_2340585
Guinea pig polyclonal anit-VGluT2 (1:100)	Millipore Sigma	AB2251-I; RRID: AB_2665454
Mouse monoclonal anti-Bassoon (1:100)	Abcam	Ab82958; RRID: AB_1860018
Rabbit polyclonal anti-Homer1 (1:100)	Synaptic Systems	Cat#160 003; RRID: AB_887730
Chemicals, peptides, and recombinant proteins		
Alexa Fluor 405 NHS-ester	Thermo Fisher Scientific	Cat#A30000
Alexa Fluor 647 NHS-ester	Thermo Fisher Scientific	Cat#A20006
Atto 488 NHS-ester	ATTO-TEC GmbH	AD 488–31
Catalase from bovine liver	Sigma-Aldrich	C1345
Chloroform	Sigma-Aldrich	Cat#288306
Cy-3B Mono NHS-ester	Cytiva	PA63101
Cysteamine	Sigma-Aldrich	Cat#30070
DY-749P1 NHS-ester	Dyomics GmnH	Cat#749P1-01
Dulbecco's Phosphate Buffered Saline	Sigma-Aldrich	D8662
Ethanol	Pharmco	Cat#111000200C1GL
FluoSpheres Infrared (715/755)	Invitrogen	Cat#F8799
FluoSpheres Orange (540/560)	Invitrogen	Cat#F8809
D-(+)-Glucose	Sigma Aldrich	Cat#G7528
Glucose Oxidase	Sigma-Aldrich	G2133
Glutaraldehyde 70%, EM grade	Electron Microscopy Sciences	Cat#16360
Normal Donkey Serum	Jackson ImmunoResearch	Cat#017-000-121
Paraformaldehyde 16%, EM grade	Electron Microscopy Sciences	Cat#15710
Sodium azide	Sigma-Aldrich	S2002
Sodium chloride	Sigma-Aldrich	S9888
Sodium hydroxide pellets	Sigma-Aldrich	Cat#567530
Tris-base (Trizma-base)	Sigma-Aldrich	T8524
Triton X-100	Sigma-Aldrich	Cat#11332481001
Critical commercial assays		
UltraBed Kit	Electron Microscopy Sciences	Cat#14310
Experimental models: Organisms/strains		
Mouse: C57BL/6J Age: 2–8 days; Sex: M/F	The Jackson Laboratory	Cat#000664
Mouse: β2-nAChR $^{-/-}$Age: 2–8 days; Sex: M/F	Burbridge et al.[104]	N/A
Oligonucleotides		
Primer: nAChR forward: CAGGCGTT ATCCACAAAGACAGA	Burbridge et al.[104]	N/A
Primer: nAChR reverse: TTGAGGGG AGCAGAACAGAATC	Burbridge et al.[104]	N/A
Primer: nAChR mutant reverse: ACTTGGGTTTGGGCGTGTTGAG	Burbridge et al.[104]	N/A

(*Continued on next page*)

Continued

REAGENT or RESOURCE	SOURCE	IDENTIFIER
Software and algorithms		
3D-DAOSTORM analysis (single-molecule localization fitting code); version 2.1	Babcock et al.[105]	https://github.com/ZhuangLab/storm-analysis
Deep-learning-based single molecule localization distribution estimation code	Developed for the current manuscript (Speer Laboratory)	https://github.com/SpeerLab/Single-molecule-localization-prediction-in-3D
Fiji (ImageJ)	Schindelin et al.[106]	https://fiji.sc
MATLAB	MathWorks	https://mathworks.com
Python3	Python	https://www.python.org
Rstudio	Posit	https://posit.co/
SPSS	IBM	https://www.ibm.com/products/spss-statistics
STORM acquisition control code (packages include hal4000.py, steve.py, and dave.py); version V2019.06.28	Zhuang Laboratory, Harvard University	https://github.com/ZhuangLab/storm-control
Other		
5-min Epoxy in DevTube	Jenson Tools	Cat#14250
BEEM embedding capsules	Electron Microscopy Sciences	Cat#70020-B
Coverslip No. 1.5 (24 mm × 30 mm)	VWR	Cat#48404–467
Custom-built STORM microscope	Babcock et al.[105]; Vatan et al.[36]	Information on our build is available from the lead contact
Microscope slides	VWR	Cat#16004–422

RESOURCE AVAILABILITY

Lead contact

Further information and requests for resources and reagents should be directed to and will be fulfilled by the lead contact, Colenso M. Speer (cspeer@umd.edu).

Materials availability

This study did not generate new unique reagents.

Data and code availability

- Super-resolution image datasets and any additional information required to reanalyze the reported data will be provided by the lead contact on request.
- All original code for STORM data analysis has been deposited at GitHub and is publicly available.
- Any additional information required to reanalyze the data reported in this paper is available upon request.

EXPERIMENTAL MODEL AND SUBJECT DETAILS

Animals

Wild-type C57BL/6J mice used in this study were purchased from the Jackson Laboratory (Stock Number 000664). $\beta2^{-/-}$ mice were a generous gift of Dr. Michael C. Crair (Yale School of Medicine). All experimental procedures were performed in accordance with an animal study protocol approved by the Institutional Animal Care and Use Committee (IACUC) at the University of Maryland. Animals were housed under standard conditions in a controlled facility under a 12 h light/12 h dark cycle with food/water available *ad libitum*. Neonatal male and female mice were used interchangeably for all experiments. Tissue from biological replicates (n = 3 animals) was collected for each age (P2/P4/P8) from each genotype (WT and $\beta2^{-/-}$) (18 animals total). Primers used for $\beta2^{-/-}$ mice genotyping can be found in the key resources table.[104,107]

METHOD DETAILS

Eye injections

Intraocular eye injections were performed one day before tissue collection. Briefly, mice were anesthetized by inhalant isoflurane and sterile surgical spring scissors were used to gently part the eyelid to expose the corneoscleral junction. A small hole was made in the

eye using a sterile 34-gauge needle and ~0.5 μL of cholera toxin subunit B conjugated with Alexa Fluor 488 (CTB-488, ThermoFisher Scientific, Catalog Number: C34775) diluted in 0.9% sterile saline was intravitreally pressure-injected into the right eye using a pulled-glass micropipette coupled to a Picospritzer (Parker Hannifin). For control experiments to test CTB labeling efficiency, binocular injections were performed using identical volumes in each eye.

dLGN tissue preparation

Animals were deeply anesthetized with ketamine/xylazine and transcardially perfused with 5–10 mls of 37°C 0.9% sterile saline followed by 10 mls of room temperature 4% EM Grade paraformaldehyde (PFA, Electron Microscopy Sciences) in 0.9% saline. Brains were embedded in 2.5% agarose and sectioned in the coronal plane at 100 μm using a vibratome. From the full anterior-posterior series of dLGN sections (~6–8 sections) we selected the central two sections for staining in all biological replicates. These sections were morphologically consistent with Figures 134–136 (5.07–5.31 mm) of the postnatal day 6 mouse brain from Paxinos, et al., "Atlas of the developing mouse brain" Academic Press, 2020 (Figure S1A). Selected sections were postfixed in 4% PFA for 30 min at room temperature and then washed for 30–40 min in 1X PBS. The dLGN was identified by the presence of CTB-488 signals using a fluorescence dissecting microscope (Figure S1A). A circular tissue punch (~500 μm diameter) containing the dLGN was microdissected from each section using a blunt-end needle. A small microknife cut was made at the dorsal edge of the dLGN which, together with the CTB-488 signal, enabled us to identify the dLGN orientation during image acquisition (Figure S1A, also see "automated image acquisition").

Immunohistochemistry

We used a serial-section single-molecule localization imaging approach to prepare samples and collect super-resolution fluorescence imaging volumes as previously described.[36] dLGN tissue punches were blocked in 10% normal donkey serum (Jackson ImmunoResearch, Catalog Number: 017-000-121) with 0.3% Triton X-100 (Sigma-Aldrich Inc.) and 0.02% sodium azide (Sigma-Aldrich Inc.) diluted in 1X PBS for 2–3 h at room temperature and then incubated in primary antibodies for ~72 h at 4°C. Primary antibodies used were Rabbit anti-Homer1 (Synaptic Systems, Catalog Number: 160,003, 1:100) to label postsynaptic densities (PSDs), mouse anti-Bassoon (Abcam, Catalog Number AB82958, 1:100) to label presynaptic active zones (AZs), and guinea pig anti-VGluT2 (Millipore, Catalog Number AB251-I, 1:100) to label presynaptic vesicles. Following primary antibody incubation, tissues were washed in 1X PBS for 6 × 20 min at room temperature and incubated in secondary antibody solution overnight for ~36 h at 4°C. The secondary antibodies used were donkey anti-rabbit IgG (Jackson ImmunoResearch, Catalog Number 711-005-152, 1:100) conjugated with Dy749P1 (Dyomics, Catalog Number 749P1-01) and Alexa Fluor 405 (ThermoFisher, Catalog Number: A30000), donkey anti-mouse IgG (Jackson ImmunoResearch, Catalog Number 715-005-150, 1:100) conjugated with Alexa Fluor 647 (ThermoFisher, Catalog Number: A20006) and Alexa Fluor 405, and donkey anti-guinea pig IgG (Jackson ImmunoResearch, Catalog Number 706-005-148, 1:100) conjugated with Cy3b (Cytiva, Catalog Number: PA63101). Tissues were washed 6 × 20 min in 1X PBS at room temperature after secondary antibody incubation.

Postfixation, dehydration, and embedding in epoxy resin

Tissue embedding was performed as previously described.[36] Tissues were postfixed with 3% PFA +0.1% GA (Electron Microscopy Sciences) in PBS for 2 h at room temperature and then washed in 1X PBS for 20 min. To plasticize the tissues for ultrasectioning, the tissues were first dehydrated in a graded dilution series of 100% ethanol (50%/70%/90%/100%/100% EtOH) for 15 min each at room temperature and then immersed in a series of epoxy resin/100% EtOH exchanges (Electron Microscopy Sciences) with increasing resin concentration (25% resin/75% ethanol; 50% resin/50% ethanol; 75% resin/25% ethanol; 100% resin; 100% resin) for 2 h each. Tissues were transferred to BEEM capsules (Electron Microscopy Sciences) that were filled with 100% resin and polymerized for 16 h at 70°C.

Ultrasectioning

Plasticized tissue sections were cut using a Leica UC7 ultramicrotome at 70 nm using a Histo Jumbo diamond knife (DiATOME). Chloroform vapor was used to reduce compression after cutting. For each sample, ~100 sections were collected on a coverslip coated with 0.5% gelatin and 0.05% chromium potassium (Sigma-Aldrich Inc.), dried at 60° for 25 min, and protected from light prior to imaging (Figure S1A).

Imaging chamber preparation

Coverslips were chemically etched in 10% sodium ethoxide for 5 min at room temperature to remove the epoxy resin and expose the dyes to the imaging buffer for optimal photoswitching. Coverslips were then rinsed with ethanol and dH_2O. To create fiducial beads for flat-field and chromatic corrections, we mixed 715/755nm and 540/560nm, carboxylate-modified microspheres (Invitrogen, Catalog Numbers F8799 and F8809, 1:8 ratio respectively) to create a high-density fiducial marker and then further diluted the mixture at 1:750 with Dulbecco's PBS to create a low-density bead solution. Both high- and low-density bead solutions were spotted on the coverslip (~0.7 μl each) for flat-field and chromatic aberration correction respectively. Excess beads were rinsed away with dH2O

for 1–2 min. The coverslip was attached to a glass slide with double-sided tape to form an imaging chamber. The chamber was filled with STORM imaging buffer (10% glucose, 17.5μM glucose oxidase, 708nM catalase, 10mM MEA, 10mM NaCl, and 200mM Tris) and sealed with epoxy.

Imaging setup

Imaging was performed using a custom single-molecule super-resolution imaging system. The microscope contained low (4x/10x air) and high (60x 1.4NA oil immersion) magnitude objectives mounted on a commercial frame (Nikon Ti-U) with back optics arranged for oblique incident angle illumination. We used continuous-wave lasers at 488nm (Coherent), 561nm (MPB), 647nm (MPB), and 750nm (MPB) to excite Alexa 488, Cy3B, Alexa 647, and Dy749P1 dyes respectively. A 405 nm cube laser (Coherent) was used to reactivate Dy749P1 and Alexa 647 dye photoswitching. The microscope was fitted with a custom pentaband/pentanotch dichroic filter set and a motorized emission filter wheel. The microscope also contained an IR laser-based focus lock system to maintain optimal focus during automatic image acquisition. Images were collected on 640*640-pixel region of an sCMOS camera (ORCA-Flash4.0 V3, Hamamatsu Photonics) with a pixel size of ~155 nm.

Automated image acquisition

Fiducials and tissue sections on the coverslip were imaged using the low magnification objective (4X) to create a mosaic overview of the specimen. Beads/sections were then imaged at high-magnification (60X) to select regions of interest (ROIs) in the Cy3B and Alexa 488 channels. Before final image acquisition, laser intensities and the incident angle were adjusted to optimize photoswitching for STORM imaging and utilize the full dynamic range of the camera for conventional imaging.

Low-density bead images were taken in 16 partially overlapping ROIs. 715/755nm beads were excited using 750 nm light and images were collected through Dy749P1 and Alexa 647 emission filters. 540/560nm beads were excited using a 488 nm laser and images were collected through Alexa 647, Cy3B, and Alexa 488 emission filters. These fiducial images were later used to generate a non-linear warping transform to correct chromatic aberration. Next, ROIs within each tissue section were imaged at conventional (diffraction-limited) resolution in all four-color channels sequentially.

Following conventional image acquisition, a partially overlapping series of 9 images were collected in the high-density bead field for all 4 channels (Dy749P1, Alexa 647, Cy3B, and Alexa 488). These images were later used to perform a flat-field image correction of non-uniform laser illumination across the ROIs. Another round of bead images was taken as described above in a different ROI of the low-density bead field. These images were later used to confirm the stability of chromatic offsets during imaging. All ROIs within physical sections were then imaged by STORM for Dy749P1 and Alexa 647 channels. Images were acquired using a custom progression of increasing 405nm laser intensity to control single-molecule switching. 8000 frames of Dy749P1 channel images were collected (60 Hz imaging) followed by 12,000 frames of Alexa 647 channel images (100 Hz). In a second imaging pass, the same ROIs were imaged for Cy3B and Alexa 488 channels, each for 8000 frames (60 Hz).

We imaged the ipsilateral and contralateral ROIs separately in each physical section of the dLGN. For consistency of ROI selection across biological replicates at each age, we identified the dorsal-ventral (DV) axis of the dLGN and selected ROIs within the center (core region) at 2/5 (ipsilateral ROI) and 4/5 (contralateral ROI) of the full DV length (Figure S1A).

Image processing

Single-molecule localization was performed using a previously described DAOSTORM algorithm.[105] Molecule lists were rendered as 8-bit images with 15.5 nm pixel size where each molecule is plotted as an intensity distribution with an area reflecting its localization precision. Low-density fiducial images were used for chromatic aberration correction. We localized 715/755 beads in Dy749P1 and Alexa 647 channels, and 540/560 beads in Alexa 647, Cy3B, and Alexa 488 channels. A third-order polynomial transform map was generated by matching the positions of each bead in all channels to the Alexa 647 channel. The average residual error of bead matching was <15 nm for all channels. The transform maps were applied to both 4-color conventional and STORM images. Conventional images were upscaled (by 10X) to match the STORM image size. The method to align serial sections was previously described.[36] STORM images were first aligned to their corresponding conventional images by image correlation. To generate an aligned 3D image stack from serial sections using Fiji,[106] we normalized the intensity of all Alexa 488 images and used these normalized images to generate both rigid and elastic transformation matrices for all four-color channels of both STORM and conventional data. The final image stack was then rotated and cropped to exclude incompletely imaged edge areas. Images of the ipsilateral regions were further cropped according to CTB-488 signals to exclude contralateral areas.

Cell body filter

The aligned STORM images had non-specific labeling of cell bodies in Dy749P1 and Alexa 647 channels corresponding to Homer1 and Bassoon immunolabels. To limit synaptic cluster identification to the neuropil region we identified cell bodies based on their Dy749P1 signal and excluded these regions from further image processing. STORM images were convolved with a Gaussian function ($\sigma = 140$ nm) and then binarized using the lower threshold of a two-level Otsu threshold method. We located connected components in the thresholded images and generated a mask based on components larger than e^{11} voxels. Because cell body clusters were orders of magnitude larger than synaptic clusters, the cell body filter algorithm was robust to a range of size thresholds. The mask was applied to images of all channels to exclude cell body areas.

Eye-specific synapse identification and quantification

To correct for minor variance in image intensity across physical sections, we normalized the pixel intensity histogram of each section to the average histogram of all sections. Image histograms were rescaled to make full use of the 8-bit range. Using a two-level Otsu threshold method, the conventional images were thresholded into three classes: a low-intensity background, low-intensity signals above the background representing non-synaptic labeling, and high-intensity signals representing synaptic structures. The conventional images were binarized by the lower two-level Otsu threshold, generating a mask for STORM images to filter out background signals. STORM images were convolved with a Gaussian function (σ = 77.5 nm) and thresholded using the higher two-level Otsu threshold. Following thresholding, connected components were identified in three dimensions using MATLAB 'conncomp' function. A watershedding approach was applied to split large clusters that were improperly connected. Clusters were kept for further analysis only if they contained aligned image information across two or more physical sections. We also removed all edge synapses from our analysis by excluding synapses that did not have blank image data on all adjacent sides. To distinguish non-specific immunolabeling from true synaptic signals, we quantified two parameters for each cluster: cluster volume and cluster signal density calculated by the ratio of within-cluster pixels with positive signal intensity in the raw STORM images. Two separate populations were identified in 2D histograms plotted from these two parameters. We manually selected the population with higher volumes and signal densities representing synaptic structures. To test the robustness of the manual selection, we performed multiple repeated measurements of the same data and discovered a between-measurement variance of <1% (data not shown).

To identify paired pre- and postsynaptic clusters, we first measured the centroid-centroid distance of each cluster in the Dy749P1 (Homer1) and Alexa 647 (Bassoon) channels to the closest cluster in the other channel. We next quantified the signal intensity of each opposing synaptic channel within a 140 nm shell surrounding each cluster. A 2D histogram was plotted based on the measured centroid-centroid distances and opposing channel signal densities of each cluster. Paired clusters with closely positioned centroids and high intensities of apposed channel signal were identified using the OPTICS algorithm. In total we identified 49,414 synapses from WT samples (3 samples each at P2/P4/P8, 9 total samples) and 33,478 synapses in $\beta 2^{-/-}$ mutants (3 samples each at P2/P4/P8, 9 total samples). Retinogeniculate synapses were identified by pairing Bassoon (Alexa 647) clusters with VGluT2 (Cy3B) clusters using the same method as pre/post-synaptic pairing. Synapses from the right eye were identified by pairing VGluT2 clusters with CTB (Alexa 488) clusters. The volume of each cluster reflected the total voxel volume of all connected voxels, and the total signal intensity was a sum of voxel intensity within the volume of the connected voxels.

VGluT2 population analysis

To identify 'small' versus 'large' VGluT2 clusters in each sample, we used the MATLAB 'histfit' function to smooth the VGluT2 cluster volume histogram by fitting it to the kernel density distribution. The smoothed curve was then fit to the equation:

$$f(x) = a_1 * e^{-\left(\frac{x-b_1}{c_1}\right)^2} + a_2 * e^{-\left(\frac{x-b_2}{c_2}\right)^2}$$

with the following boundary conditions:

$$a_1, a_2 > 0$$

$$b_1, b_2 < 0$$

The peak positions were determined by the fitting results of b_1 and b_2.

Analysis of vesicles associated with the AZ

AZ-associated vesicles were quantified by VGluT2 signal volume and signal intensity within 48 nm proximity to its paired Bassoon cluster ($\sim$ length of 3 pixels in STORM images and slightly larger than the diameter of a synaptic vesicle). AZ-associated VGluT2 signal volume linearly increased when progressively increasing the shell size (16-32-48–64 nm; data not shown). Synapses with no VGluT2 signal inside a 48 nm AZ shell were defined as 'null' synapses.

SSD analysis based on voxel intensity distributions

SSDs were identified by applying a watershedding algorithm (MATLAB) on interpolated synaptic cluster images with 15.5 nm isotropic voxels. The image was convolved with a Gaussian filter (σ = 24 nm for the 647 channel and 32 nm for the 750 channel) before watershedding. Watershedding parameters were initially chosen based on visual inspection of SSD segmentation output on a subset of randomly selected synaptic clusters. To further validate the output, watershedding parameters were applied to shuffled pixel intensity distributions within convex hulls of all synaptic clusters. In shuffled controls, fewer than 10% of clusters showed any SSDs (data not shown).

To quantify the transsynaptic SSD displacement, we applied principal component analysis (PCA) to each pre/postsynaptic cluster independently to find the unit vector $\vec{v_1}$ perpendicular to each cluster plane based on the first two principal components. Paired Bassoon and Homer1 clusters were included in the transsynaptic SSD displacement analysis if the offset angle between their individual $\vec{v_1}$ vectors was <30° indicating parallel pre/postsynaptic alignment. We then measured a second vector $\vec{v_2}$ that connected the

weighted centroid of each presynaptic (Bassoon) SSD to its closest neighboring postsynaptic (Homer1) SSD. When an individual Homer1 SSD paired with multiple Bassoon SSDs, the pair with smallest distance was maintained in the analysis.

The transsynaptic SSD displacement was calculated by:

$$\sqrt{\left|\overrightarrow{(v_2)}\right|^2 - \left|\overrightarrow{(v_1)}\cdot\overrightarrow{(v_2)}\right|^2}$$

The randomized transsynaptic SSD displacement was calculated from the same equation above, using shuffled SSD centroid distributions within the convex hull of each Homer1 cluster while maintaining the original presynaptic SSD positions.

SSD analysis based on single molecule localization distributions

For each synaptic cluster identified in image-based analysis we performed an SSD analysis based on single molecular localization distributions. After STORM image acquisition, 2D single molecule distribution (ground truth data) was determined for each individual physical sections. We converted molecule distributions to image pixel intensity values (2D STORM images), which were then processed for drift correction, chromatic alignment correction, and 3D elastic registration to generate final STORM volumetric image stacks. To retrieve the single molecule distributions for SSD identification, we developed a machine learning approach to reconstruct single molecule positions in 3D from volumetrically aligned STORM image stacks. First, to establish a relationship between image voxel intensity and single molecule distributions, we estimated the nearest-neighbor-averaged (NNA) number of single molecules present in each pixel within 2D STORM images of synaptic clusters. We sampled individual image clusters from non-volumetrically-aligned 2D STORM images, for which we have corresponding pixel intensity distributions and ground truth single molecule localizations. We used a linear function to fit the relationship between NNA pixel intensity and NNA number of molecules for each pixel, enabling the estimation of NNA molecules per pixel based on NNA pixel intensity.

In step two, we used a Convolutional Neural Network (CNN) to refine the estimation of NNA molecules per pixel. Individual 2D STORM image clusters were centered in a fixed-size tile and fed to the CNN as inputs. The output of the network was an ordered list of residual error between the predicted number of molecules (from step one) and the actual number of molecules (from the ground truth STORM localization lists) present in each pixel. Within a dataset of >14,000 input-output pairs, 90% of the dataset was used for the training process and the remaining 10% was used for validation. In the training process, the CNN minimized the training error which is the sum of the mean-squared prediction error for pixels in all clusters. The training process significantly decreased the training error, indicating that the CNN improved upon the initial molecule distribution estimation from step one (data not shown). Predictions on the validation dataset also showed decreased prediction error. The trained CNN was used to predict the number of molecules inside each pixel of synaptic clusters within volumetrically-aligned STORM image stacks. For 3D reconstruction, the positions of predicted molecules in each pixel were then assigned randomly in a 15.5 × 15.5 × 70 nm voxel.

In step three, we identified SSDs based on the local density of reconstructed 3D molecular distributions for each synaptic cluster. A DBSCAN clustering algorithm was used to predict SSDs within each 3D cluster. We optimized DBSCAN parameters to produce subcluster identification with good visual agreement with SSD analysis based on image voxel intensity distribution. To avoid false positive detection of SSDs, we applied the same DBSCAN analysis to shuffled data (randomized localization positions within each cluster convex hull) and found small SSDs with few localizations (mean 6–7 localizations/SSD). From this, we set a threshold for SSD selection in the original data 3σ above the average number of molecules in small SSDs from the shuffled analysis. We then analyzed the volumetrically aligned datasets to compute the number of SSDs within each synapse and the volume of each SSD.

To evaluate whether SSDs identified from the predicted single molecule distributions reflect ground truth SSDs, we randomly selected 50,000 clusters from 2D STORM images and applied the trained CNN model to generate predicted molecule localizations. We then applied DBSCAN analysis using the same parameters to the ground truth localizations and CNN predicted molecule localizations. After matching the closest neighboring SSDs from the two datasets and calculating the SSD centroid offsets, we found 88% of Bassoon SSDs and 82% of Homer1 SSDs in the ground truth data were paired with an identified SSDs in the CNN predicted data with a centroid offset of <70 nm (thickness of the physical section). We quantified the offsets between all closest paired SSDs in the two datasets to show the total error in SSD identification (Figure S4B). These were compared with randomized data generated by assignment of each SSD centroid to a random position within the full CNN predicted single molecule distribution (Figure S4B).

Homer1 population analysis from single molecule localization distributions

To partition Homer1 SSDs into large and small populations, we fit the smoothed histogram of SSD volume with a two-peak Gaussian function (see section: "VGluT2 population analysis"). The intersection of the two Gaussian functions was used as the threshold to partition small vs. large Homer1 SSDs.

QUANTIFICATION AND STATISTICAL ANALYSIS

Statistical analysis was performed using SPSS. Plots were generated by SPSS or R (ggplot2). The statistical details can be found in the figure legends. For all measurements in this paper, we analyzed n = 3 biological replicates (individual mice) for each genotype (WT and $\beta 2^{-/-}$) at each age (P2, P4, and P8). We used a linear mixed model to compare Homer1, Bassoon, or VGluT2 SSD/cluster volumes and total signal intensity. In each comparison, the age or eye-of-origin was the fixed main factor and biological replicate IDs

were nested random factors. Pairwise comparisons among main factor groups were performed by a post-hoc Bonferroni's test. Cluster densities, average SSD numbers per cluster, and average transsynaptic SSD displacements were presented as mean ± SEM values in line plots and were compared by one-way ANOVA tests with a post-hoc Tukey's test. In violin plots, each violin showed the distribution of grouped data from all biological replicates from the same condition. Each black dot represents the median value of each biological replicate and the horizontal black line represents the group median. Black lines connect measurements of CTB(+) and CTB(−) populations from the same biological replicate. Asterisks in all figures indicate statistical significance: *$p < 0.05$, **$p < 0.01$, ***$p < 0.001$.

Cell Reports, Volume *42*

Supplemental information

The synaptic basis of activity-dependent eye-specific competition

Chenghang Zhang, Swapnil Yadav, and Colenso M. Speer

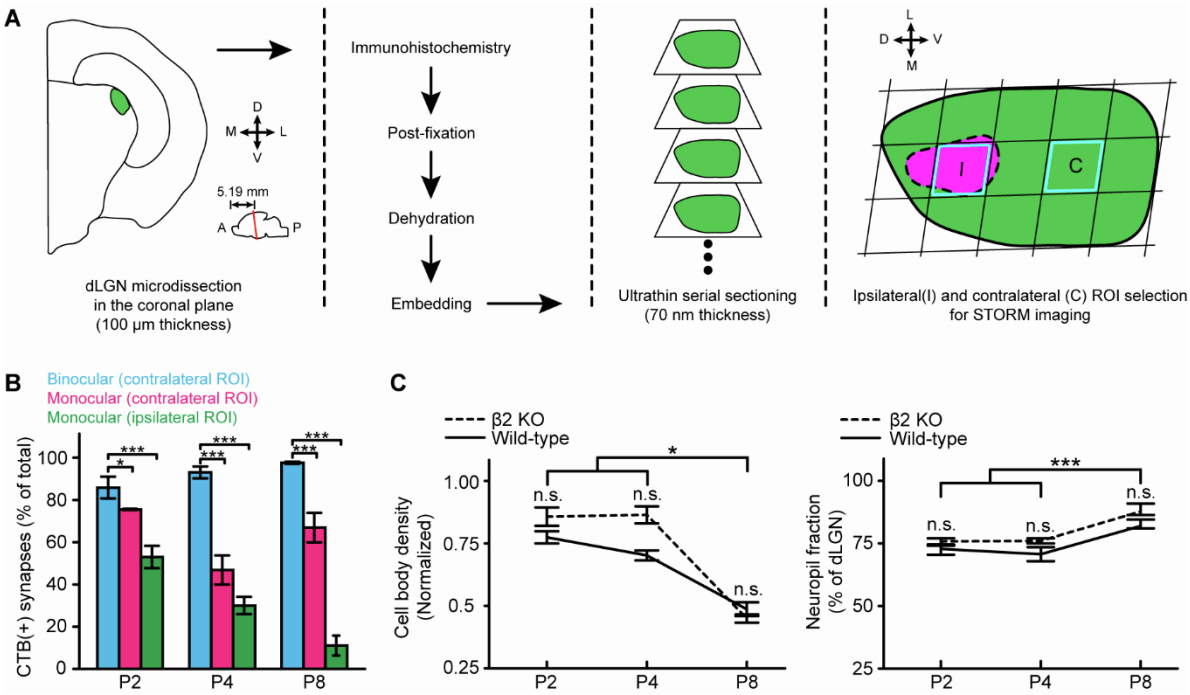

Supplemental Figure 1: High efficiency eye-specific synapse labeling and normal dLGN cytoarchitectural development in β2$^{-/-}$ mice, related to Figure 1.

(**A**) Overview of sample preparation and image acquisition. The mouse brain was dissected (100 µm thick coronal sections) and dLGN tissue (green) was microdissected for immunohistochemistry, post-fixation, dehydration, embedding, and serial ultrasectioning (70 nm section thickness). The right panel shows the positions of selected ipsilateral and contralateral ROIs. Magenta and green indicate eye-specific regions innervated by axons of the ipsilateral eye and contralateral eye in adult mice. The grid lines show the ipsilateral/contralateral ROI selection within the dLGN center (along the ML axis) at 2/5 and 4/5 distance respectively (along the maximal DV axis).

(**B**) CTB labeling efficiency in retinogeniculate synapses during development. The bar plot shows the fraction of VGluT2 clusters (retinogeniculate synapses) co-labeled with CTB signals in binocular or monocular injection experiments for WT mice over development. Error bars reflect means ± SEMs from N = 3 biological replicates at each age. Statistical analysis was performed using a one-way ANOVA with a post-hoc Tukey's test. *P<0.05, ***P<0.001.

(**C**) Normal dLGN cytoarchitecture development in WT and β2$^{-/-}$ mice. Line plots show the cell body density (left panel) and neuropil fraction (right panel) measurements combined from ipsilateral and contralateral ROIs. The cell body densities were normalized to the total imaging volume for each ROI. Error bars reflect means ± SEMs for N = 3 biological replicates for each age and genotype. Statistical analysis was performed using a one-way ANOVA with a post-hoc Tukey's test. *P<0.05. ***P<0.001. 'n.s.' = not significant.

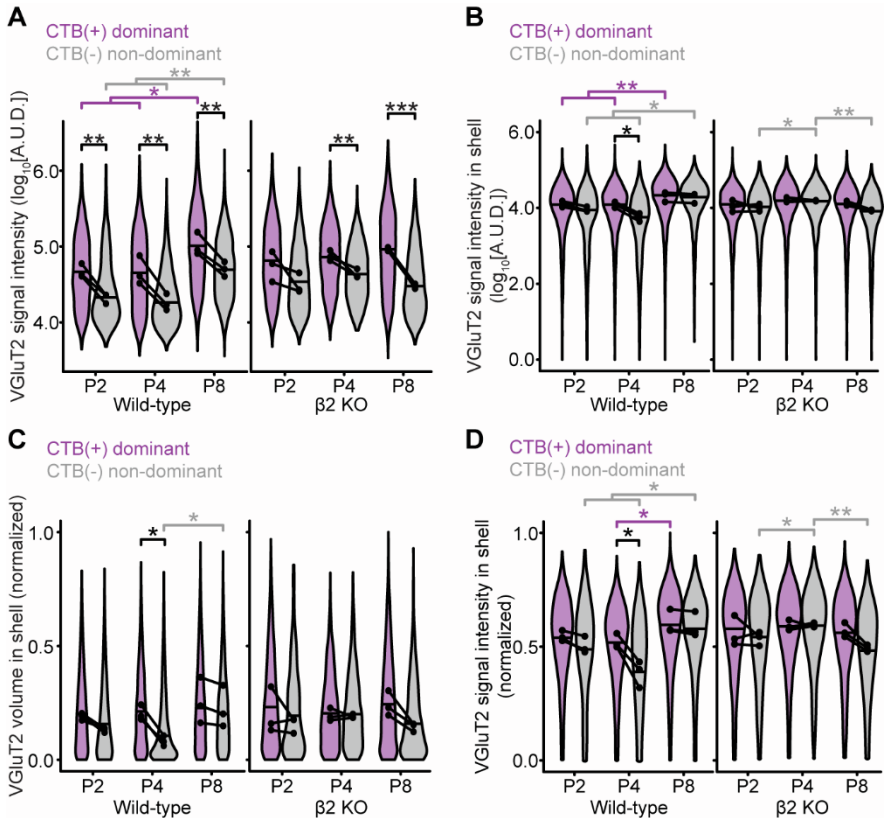

Supplemental Figure 2: Developmental maturation of VGluT2 cluster signal intensity and within-shell VGluT2 properties during eye-specific competition, related to Figure 2.

(A) Eye-specific developmental changes in VGluT2 signal intensity in WT (left panel) and $\beta2^{-/-}$ mice (right panel). For all results in A-D, the violin plots show the grouped distribution from 3 biological replicates imaged in the contralateral ROI. Horizontal lines show the median values of the grouped data. Black dots reflect the individual median values for each biological replicate. Black lines between CTB(+) and CTB(-) populations represent data collected from the same biological replicate sample. Statistical analysis was performed using a mixed model ANOVA where the age or eye-of-origin was the fixed main factor and the biological replicate ID was a random nested factor. Pair-wise comparisons between ages were performed using a post-hoc Bonferroni's test. Black asterisks indicate statistical comparison between eye-specific CTB(+) and CTB(-) clusters. Purple asterisks indicate statistical comparisons between CTB(+) clusters across ages. Gray asterisks indicate statistical comparisons between CTB(-) clusters across ages. *P < 0.05, **P < 0.01.

(B) Eye-specific VGluT2 signal intensity at the AZ in WT (left panel) and β2-/- mice (right panel) across development.

(C) Eye-specific VGluT2 volume at the AZ in WT (left panel) and β2-/- mice (right panel) across development normalized to the AZ volume.

(D) Eye-specific VGluT2 signal intensity at the AZ in WT (left panel) and β2-/- mice (right panel) across development normalized to the AZ volume.

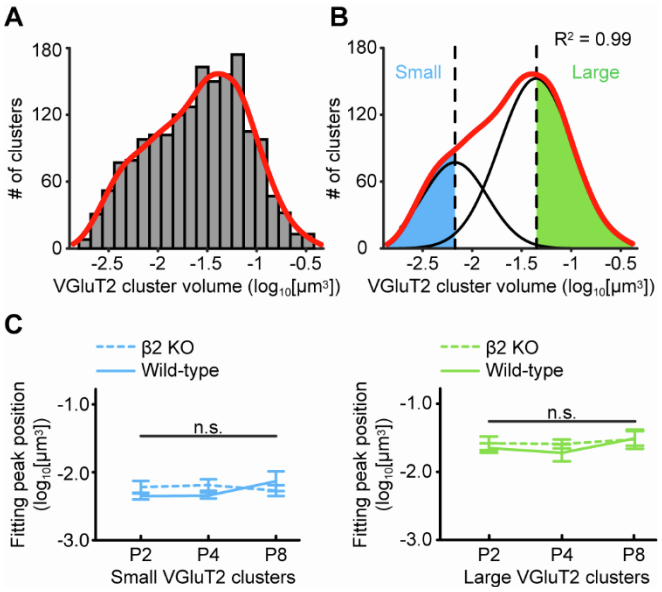

Supplemental Figure 3: Identification of small versus large VGluT2 cluster populations during eye-specific segregation, related to Figure 3.

(**A**) Histogram of VGluT2 cluster volumes in the contralateral ROI. Gray bars show a CTB(+) VGlUT2 cluster volume histogram from a representative WT P8 sample. The histogram was fit with the kernel density estimation as a smoothed distribution (red line).

(**B**) Definition of small versus large VGluT2 clusters in the same sample as (A). The smoothed histogram (red line same as A) was fit by a 2-peak Gaussian function (black lines).The peak position of each Gaussian function (black dashed lines) defined small (blue) and large (green) clusters respectively. R^2 value reflects the coefficient of determination.

(**C**) Cluster fitting was consistent across all ages and genotypes. The line plots show the smaller Gaussian peak position (left panel) and larger Gaussian peak position (right panel) for WT (solid lines) and $\beta2^{-/-}$ (dashed lines) mice. Error bars reflect means ± SEMs from N = 3 biological replicates for each age and genotype. Statistical analysis was performed using a one-way ANOVA with a post-hoc Tukey's test. 'n.s' = not significant.

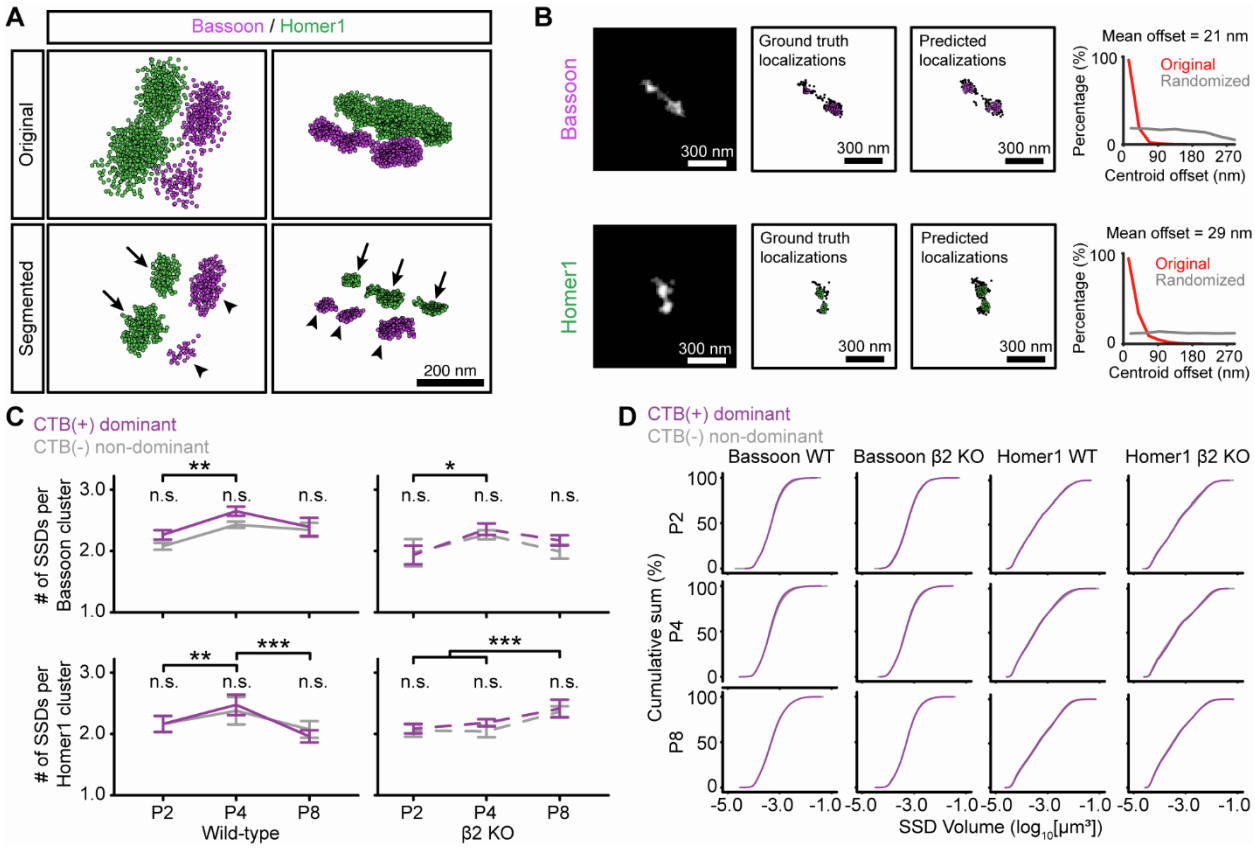

Supplemental Figure 4: Activity-dependent SSD development from localization-based analysis, related to Figure 4.

(**A**) Subsynaptic domain (SSD) identification in the localization-based analysis. Single molecule localizations (individual dots) within each retinogeniculate synapse were predicted using a deep learning-based method (top panels, see STAR Methods). SSDs were identified by density-based spatial clustering of applications with noise (DBSCAN) analysis of Bassoon (magenta, arrowheads) and Homer1 (green, arrows) localizations. Representative synapses are the same as those shown in Figure 4A.

(**B**) Validation of SSD identification using CNN-predicted single molecule distributions. Bassoon (top panels) and Homer1 (bottom panels) clusters were randomly selected from the WT P8 dataset. Representative 2D cluster images (single 70 nm sections) are shown in grayscale and their corresponding ground truth and CNN-predicted localizations are shown as dots on the right of each image. Single molecule localizations within identified SSDs are shown as colored dots. SSDs identified in ground truth localizations and predicted localizations were paired by their weighted centroid position (see STAR Methods). The right panels show the distribution of paired SSD weighted centroid offsets (linear distance measurement, red lines) between the two datasets (mean offsets were ~21 and 29 nm for Bassoon/Homer1 respectively). The paired SSD offsets were significantly smaller than randomized controls in which postsynaptic SSD positions were generated by random centroid assignment within the predicted localization distribution.

(C) Changes in the average number of SSDs per synaptic cluster during development in localization-based analysis. The line graphs show the SSD number in Bassoon (top panels) and Homer1 (bottom panels) in WT (left panels) and $\beta2^{-/-}$ (right panels) mice over development. Purple lines show CTB(+) dominant-eye synapses while gray lines show CTB(-) non-dominant-eye synapses. Error bars reflect means ± SEMs from N = 3 biological replicates imaged in the contralateral ROI. Statistical analysis was performed using a one-way-ANOVA with a post-hoc Tukey's test. *P < 0.05, **P < 0.01. ***P < 0.001. 'n.s.' = not significant.
(D) Eye-specific comparison of Bassoon and Homer1 SSD volume in localization-based analysis. Cumulative sum distributions are shown for CTB(+) (purple lines) and CTB(-) (gray lines) eye-specific clusters. Plots show WT Bassoon (first column), WT $\beta2^{-/-}$ (second column), WT Homer1 (third column), and $\beta2^{-/-}$ Homer1 (fourth column) as a function of age (rows). Statistical analysis was performed using a mixed model ANOVA where the eye-of-origin was the fixed main factor and the biological replicate ID was a random nested factor. There were no significant eye-specific differences in SSD volume for Bassoon or Homer1 as a function of age or genotype.